

# Bluff body drag manipulation using pulsed jets and Coanda effect

Diogo Barros<sup>1,2,†</sup>, Jacques Borée<sup>1</sup>, Bernd R. Noack<sup>1,3</sup>  
Andreas Spohn<sup>1</sup> and Tony Ruiz<sup>2</sup>

<sup>1</sup>Institut Pprime, UPR-3346 CNRS, Université de Poitiers, ENSMA  
Futuroscope Chasseneuil, 86000, France.

<sup>2</sup>PSA Peugeot-Citroën, Centre Technique de Vélizy, Vélizy-Villacoublay, 78943, France.

<sup>3</sup>Institut für Strömungsmechanik, Technische Universität Braunschweig  
Hermann-Blenck-Straße 37, D-38108 Braunschweig, Germany.

(Received ?; revised ?; accepted ?. - To be entered by editorial office)

The impact of fluidic actuation on the wake and drag of a 3D blunt body is experimentally investigated. The wake is forced by jets pulsed tangentially to the main flow with variable frequency and velocity. Depending on the forcing conditions, two flow regimes can be identified. First, for a broadband range of frequencies comprising the natural wake instabilities, the convection of the jet structures enhances wake entrainment, shortening the recirculating flow length with an augmentation of the bluff body drag. Further increase of the actuation frequency induces a wake *fluidic boat-tailing* by shear-layer deviation. It additionally lowers turbulent intensity and entrainment of high momentum fluid in the shear layer, leading to an overall reduction of the wake fluctuating kinetic energy. The association of both mechanisms is responsible for a raise of base pressure and decrease of the model's drag. The physical features of such regimes are discussed on the basis of drag, pressure and velocity measurements at several upstream conditions and control parameters. By adding curved surfaces at the jet outlets to take advantage of the so-called Coanda effect, periodic actuation can be further reinforced leading to drag reductions of about 20% in unsteady regime. In general, the unsteady Coanda blowing not only intensifies the base pressure recovery but also preserves the effect of unsteady high frequency forcing on the turbulent field. The present results encourage the development of fluidic control in road vehicles' aerodynamics as well as provides a complement to our current understanding of bluff body drag and its manipulation.

**Key words:**

## 1. Introduction

Drag reduction of bluff bodies has become a major challenge for transport vehicles due to increasing need for reducing fuel consumption and carbon pollution. For example, more than 50 % of a vehicle's engine power is necessary to overcome its aerodynamic drag on a highway (Hucho & Sovran 1993). The drag of cars is principally due to their shape, causing significant pressure differences between their front and rear surfaces. In contrast to streamlined bodies, the flow massively separates leading to the formation of a recirculating flow with reduced pressure. The wake flow of simplified square back road vehicles was extensively studied in the past (Ahmed *et al.* 1984) and reviewed by recent

† Email address for correspondence: diogo.barros@ensma.fr

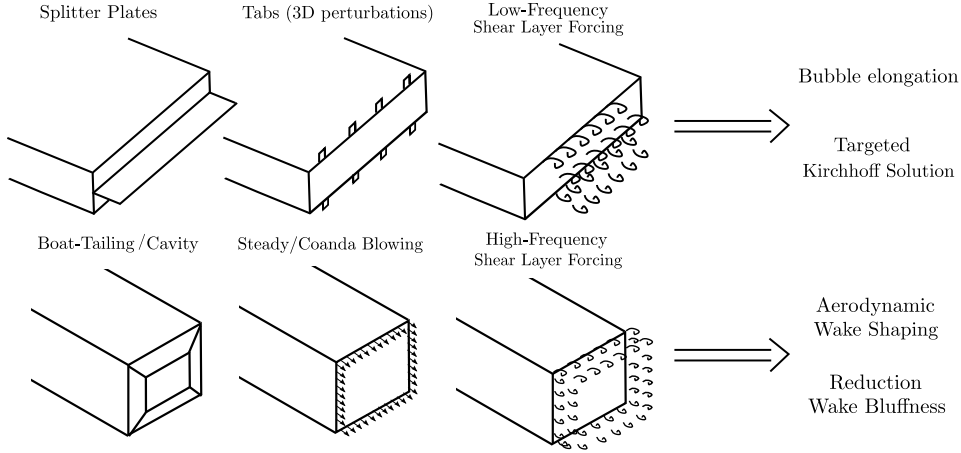


FIGURE 1. Overview of representative drag reducing devices for blunt body wakes.

literature detailing its unsteady features (Grandemange *et al.* 2013; Choi *et al.* 2014). The wake contains low energy recirculating flow surrounded by free shear layers. According to Huerre & Monkewitz (1990), these shear layers convectively amplify flow perturbations while the absolute instability of the recirculating flow produces self-sustained large-scale oscillations.

Within this context, flow control turned out to be an efficient way to modify bluff body wakes with the aim to increase the baseline pressure (Choi *et al.* 2008). Figure 1 summarizes the main drag reducing devices for two and three-dimensional blunt body wakes. The goal is either to reduce wake entrainment to elongate the formation region towards the Kirchhoff solution or to decrease the cross section of the wake in order to modify the bubble’s aspect ratio and increase the pressure recovery (Roshko 1955; Gerrard 1966).

The former goal was achieved mainly for nominally 2D flows. A damping of the strong periodic motions in these wakes is effective either by the use of splitter plates (Bearman 1965) or by three-dimensional perturbations using tabs devices (Park *et al.* 2006). Moreover, active flow control by pulsating and zero-net-mass-flux jets reveals positive effects on the model’s drag (Pastoor *et al.* 2008; Chaligné *et al.* 2013). On the contrary, these strategies have not been proven to be effective in 3D flows, where the strong vortex shedding is absent. In 3D wakes, pressure recovery is obtained by boat-tailing and cavity effects of the body shape (Choi *et al.* 2014) or by producing flow deflection through steady jets associated or not with a Coanda effect (Englar 2001; Littlewood & Passmore 2012; Pfeiffer & King 2012). For practical applications, these control techniques show limitations related to power cost and geometrical constraints.

In this sense, we explore the possibility to decrease both constraints by deviating the flow through unsteady shear layer forcing and Coanda effects. Perturbing shear-layers has been the subject of a significant body of work (Ho & Huerre 1984). The transition from the separated boundary-layers to a self-similar shear-layer is highly sensitive to the frequency and the strength of perturbations (Fiedler 1998). In particular, periodic forcing of initially formed shear-layers shows a wide spectrum of effects.

By local forcing with time period close to the shear-layer most amplified frequencies, Chun & Sung (1996) were capable to drastically reduce the recirculating length of a backward-facing step flow with low-amplitude actuation. An increase of the actuation

frequency, however, promoted an enlargement of the recirculating flow behind the step. Similar results were obtained from the numerical simulations of Dandois *et al.* (2007) and Dahan *et al.* (2012) around ramps and steps, where high-frequency forcing increases the size of the bubble. Dandois *et al.* (2007) concluded that the deadwater region significantly decreases at low-frequency actuation close to the flow instabilities. In this situation, the perturbed shear-layers presented high turbulent kinetic energy and production. On the other hand, by augmenting the forcing frequency, the scenario is inverted and a stabilization of the velocity fluctuations is noted at some regions of the shear-layer. The length of the bubble is extended and a lower entrainment rate along the mixing layer was suggested. Dahan *et al.* (2012) noted an increase of the base pressure of the step flow at high-frequency forcing, suggesting further applications for bluff body drag reduction.

The influence of small-scale actuation on the damping of large-scale motions has been also studied in shear-layers. In the experiments of Vukasinovic *et al.* (2010), a local increase of turbulent kinetic energy production due to actuation is followed by an important damping of velocity fluctuations in the streamwise direction. This effect has been associated to a dissipative small-scale actuation influencing notably the large-scale motions. More recently, Parezanović *et al.* (2015) exemplified the capabilities of both augmenting or decreasing the turbulent fluctuations across a canonical mixing layer by applying low or high frequency forcing, respectively.

An analysis of the time scales in periodically excited wakes is crucial to understand the base pressure modifications and the recirculating flow physics. How *low* or *high* is a determined driving frequency when compared to the wake vortex shedding? Is this frequency located in the range amplified by the shear-layer instabilities surrounding the recirculating flow? The work of Glezer *et al.* (2005) among others discussed these aspects in the light of a coupling between the forcing and the wake instabilities.

Actuation at frequencies with an order of magnitude higher than the natural vortex shedding appears a promising strategy for wake manipulation since it allows to act directly on the spreading rate of the shear layers, while the global instability modes of the flow are not amplified (Glezer *et al.* 2005). Recently, Morrison & Qubain (2009); Barros *et al.* (2014); Oxlade *et al.* (2015) applied small-scale actuation to reduce the pressure drag of axisymmetric and square-back geometries using unsteady jets. They were periodically released along the border of the rear geometry in the direction of the main flow. A virtually shaped time-averaged flow was observed by these authors and associated to a reduction of the wake cross section reducing the bluff body drag. However, the mechanisms by which the forced shear flow affects the base pressure remains to be clarified. One would be also interested in identifying the effects of low-frequency actuation on wake entrainment and drag. How does the amplification of the wake instabilities impact the baseline pressure? Are there other parameters in the wake by which we should scale the forcing frequency?

The present work aims to clarify such aspects and to bring out novel ways to manipulate bluff body drag. For that, we apply fluidic forcing by pulsing periodic jets (Cattafesta & Sheplak 2011) along the border of the trailing-edges of a square-back geometry similar to that studied by Ahmed *et al.* (1984). By varying both the frequency and amplitude of the excitation, our objective is twofold. First we identify the global effects of forcing on the model's drag. Then, we analyze the impact of control on the forced wakes to get a feedback of their dynamical changes. Secondly, we correlate the mechanisms by which the shear layer actuation modifies the wake to the base pressure changes. An experimental apparatus was designed for this study (§ 2). Some aspects of the unforced reference flow are briefly reviewed in § 3 based on past literature. A parametric study concerning the effects of both the forcing frequency and amplitude is presented in § 4 followed by

specific flow analysis of some forced wakes (§ 5, 6). We devoted § 7 to discussions related to the actuation time scales, where a conceptual scenario for high-frequency actuation is proposed. These aspects are applied in a coupled study with the Coanda effect (§ 8) to measure the impact a local change in the jet boundary conditions, which is finally succeeded by the concluding remarks (§ 9).

## 2. Experimental apparatus

In the following, we describe the experimental facility comprised of the wind-tunnel and model geometries as well as the measurement techniques used throughout the present study. Then, the pulsed jet system designed for wake manipulation is detailed. Additional information about the entire setup can be found in Barros (2015).

### 2.1. Wind-tunnel facility and model geometry

The experiments are performed inside the working section of a subsonic wind-tunnel with 2.4 m (width)  $\times$  2.6 m (height) cross-sectional area. The maximum upstream velocity  $U_o$  is about 60 ms<sup>-1</sup>. Free-stream turbulence intensities are of the order of 0.5 %. A uniform conditioning of the flow along the entire facility is achieved for velocities higher than 5 ms<sup>-1</sup>.

Figure 2(a) displays a schematic of the working section configuration. The blunt body model with height  $H = 0.297$  m, width  $W = 0.350$  m and length  $L = 0.893$  m is the same as in the study of Östh *et al.* (2014). Its front edges are rounded with a radius  $R = 0.085$  m. The bluff body is mounted over a flat plate with elliptical leading-edge to ensure an approach flow outside the ground boundary layer. The turbulent boundary layer thickness upstream the model measures  $\delta_{99\%} \sim 0.034H$ . Considering the upper area above the false floor, the overall blockage ratio is 2.2 % and no corrections are performed given this satisfactory value (West & Apelt 1982). Besides, attention is paid to the whole system lift in order to achieve an upstream flow normal to the flat plate leading-edge by the use of a downstream flap with an angle  $\alpha_{\text{flap}}$  of 5.7°. Four oval shaped supports fixed the geometric ground clearance  $G = 0.05$  m, which is approximately five times greater than the upcoming boundary layer over the floor whose shape factor is  $\bar{H} = 1.58$ . These supports are connected to a drag balance detailed in the following paragraph.

Based on the height of the model, the Reynolds number of this flow is defined as  $Re_H = U_o H \nu^{-1}$ , where  $\nu$  is the kinematic viscosity of the air at ambient temperature. Most of the results are conducted for  $U_o = 15$  ms<sup>-1</sup>, corresponding to  $Re_H = 3.10^5$ . We define the streamwise, transverse (cross-stream) and spanwise flow directions respectively by the  $x$ ,  $y$  and  $z$  axes. The origin  $O$  of the coordinate system is arbitrarily placed over the floor and at the same streamwise position of the model's rear surface. Unless otherwise specified, all physical quantities are normalized by  $U_o$ ,  $H$  and by the dynamic pressure  $q_o = 0.5\rho U_o^2$ , where  $\rho$  is the air density at ambient temperature.

### 2.2. Drag force measurements

In order to quantify the effects of unsteady pulsed jets on the drag, force measurements are obtained by the use of an in-house aerodynamic balance. This balance is designed to measure the displacement of two plates by the use of a 9217A Kistler piezoelectric high sensitive sensor for forces from 1 mN upwards. The streamwise drag moves an upper plate connected to the model's supports. This movement promotes an expansion of the sensor which is coupled to another plate fixed to the false floor structure and central support (see the setup figure for details). The measured drag force  $F_x$  is normalized by the frontal area  $S = WH$  of the bluff body and by the dynamic pressure  $q_o$  as follows:

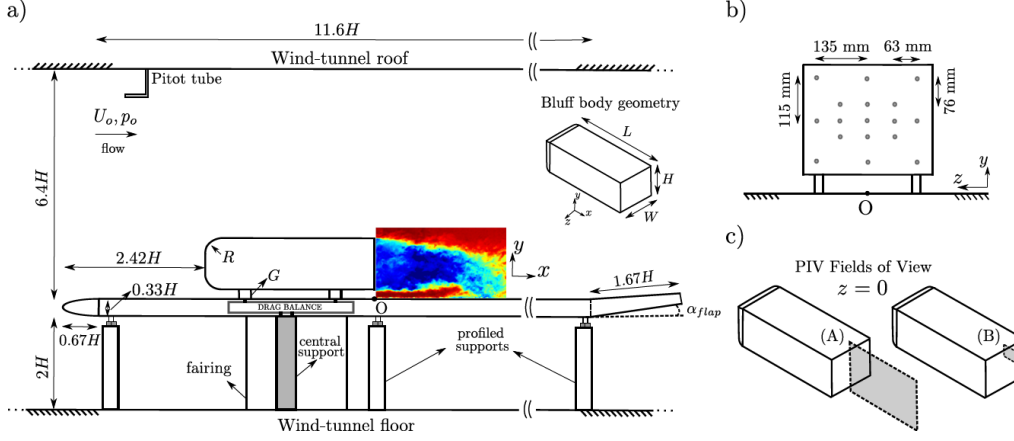


FIGURE 2. Experimental set-up. a) Wind-tunnel, flat plate dimensions and model positioning. The details of the model geometry are given by its 3D view in the inserted picture. b) Pressure taps locations used to evaluate the base pressure. c) PIV fields of view in the symmetry plane: a large window (A) to perform 2D2C PIV and a smaller window (B) for time-resolved PIV close to the upper shear layer.

$$C_x = \frac{F_x}{q_o S}, \quad (2.1)$$

where  $C_x$  is the drag coefficient.

The measured  $C_x$  is the time average of six signals each one with 10 seconds of acquisition duration. The acquisition frequency is set at 6.25 kHz by an ETEP system. A low pass filter at 1 Hz is used to obtain the time-averaged drag coefficient. As an example, at  $Re = 3.0 \times 10^5$  the drag coefficient of the reference flow equals  $C_{x_o} = 0.293 \pm 0.005$  with 95% confidence. The precision on the force measurements is  $\pm 0.07\text{N}$ . Overall, the drag coefficient is estimated to be good within less than 2% based on the standard deviations of several configurations. To quantify the drag variations with respect to the reference flow, we use the drag parameter  $\gamma_d = C_x/C_{x_o}$  which indicates an increase (resp. decrease) of drag for values greater (resp. smaller) than 1.

The measurements of drag are corrected to take into account the pulsed jet thrust generated from the wake forcing. For that, we subtract the measured force due to the jets in quiescent air.

### 2.3. Base pressure coefficient

To evaluate the pressure drag changes of the model, 17 pressure taps are installed on its rear surface as illustrated in figure 2(b). The amount of pressure taps as well as its spatial distribution is sufficient to describe the base pressure and its topology. This has been verified by the data from the large eddy simulation analyzed in Östh *et al.* (2014). The differential SensorTehcnics HCLA 02X5DB off-set pressure sensors operate with the upstream static pressure  $p_o$  as the reference value and within a range of  $\pm 250\text{ Pa}$ . We normalize the pressure by using the dynamic head  $q_o$  as:

$$C_p = \frac{p - p_o}{q_o}. \quad (2.2)$$

We define  $\langle C_p \rangle$  and  $\overline{C_p}$  as the spatial and the time averaged pressure coefficients respectively taken over the rear surface of the model and during 60 seconds of acquisition.

Albeit the wake may exhibit long time scales associated to intermittent reversals of the recirculating flow (Grandemange *et al.* 2013), the spatially and time-averaged pressure coefficient  $\langle C_p \rangle$  should not be affected according to the recent measurements from Volpe *et al.* (2015). The nominal response delay of these sensors is about 0.5 ms which enables us to perform unsteady pressure measurements as detailed in Ruiz *et al.* (2009). The acquisition frequency of the signals is set to 6.25 kHz.

The averaged base pressure for the reference flow is called  $\langle C_{p_o} \rangle$ . Based on the standard deviations from preliminary measurements of 5 minutes duration, the precision of the base pressure is calculated to be  $\pm 0.004$  corresponding to less than 3 % of  $\langle C_p \rangle$ . Similarly to the drag measurements, we define the pressure parameter  $\gamma_p = \langle C_p \rangle / \langle C_{p_o} \rangle$ : as  $C_p$  values are negatives in the recirculating flow, when  $\gamma_p < 1$  (resp.  $\gamma_p > 1$ ) the base pressure of the model increases (resp. decreases).

#### 2.4. Velocity measurements in the wake

Velocity measurements are performed in the wake by the use of particle image velocimetry (PIV) and hot-wire anemometry (HWA). Two PIV fields of view are located in the symmetry plane ( $z = 0$ ). The position of these fields is detailed in figure 2(c). A larger field (A) spans the whole wake containing entirely the recirculating flow domain. The second domain (B) corresponds to a zoom on the upper shear layer extending to  $x/H \sim 0.4$ .

The largest field of view is performed to capture the essential global modifications of the forced wake. Both the streamwise ( $u$ ) and the cross-stream or transverse ( $v$ ) velocity components of the flow are measured by two LaVision Imager pro X 4M cameras with resolution of  $2000 \times 2000$  pixels. A laser sheet is pulsed with time delays of  $120 \mu\text{s}$  (when  $U_o = 15 \text{ ms}^{-1}$ ) in the symmetry plane and image pairs are acquired at a sampling frequency of 3.5 Hz. Velocity vectors are processed with an interrogation window of  $32 \times 32$  pixels with a 50 % overlap. The resulting spatial resolution is approximately 1 % of the model's height. Ensembles of 1000-2500 independent velocity fields are used to compute first and second order statistics.

The second PIV setup enables to perform a zoom close to the upper edge of the model using high-speed PIV (HSPIV). One Photron<sup>®</sup> SA-Z 1.1 camera with a resolution of  $1024 \times 1024$  pixels was used to acquire images at a rate of 10 kHz. The laser sheet is generated by a Quantronix MESA 532 nm system. In general, the test are performed during 8 s leading to 80000 snapshots. The images are processed with an interrogation window of  $16 \times 16$  pixels and an overlap of 50 %. The final spatial resolution is  $0.003H$ .

Hot-wire measurements using a single wire probe (55P11) are acquired by a StreamlinePro Anemometer System (from Dantec Dynamics<sup>®</sup>). Typically, they are performed to quantify the boundary layer characteristics and to get spectral content in the wake downstream the closure of the recirculating flow. The HWA also serves to calibrate the exit velocity of the pulsed jet system. A 55H21 support fixes the probe to a profiled displacement system installed on the roof of the wind tunnel. The velocity measurements are sampled at 6.25 kHz and the duration of each test varies between 60 and 120 s.

#### 2.5. Pulsed jet system and forcing parameters

As stated in the Introduction, the unsteady wake forcing will be obtained by the periodic blowing of jets along the edges of the model, as illustrated in figure 3(a). The generation of pulsed jets with an exit velocity  $V_j$  is a result of a pressure difference between the external flow and a compressed air reservoir located inside the body. The volume of this cylindrical plenum chamber is 31 (liters) and its internal pressure is called the input pressure  $P_i$ .

The mass flow is driven periodically by 32 solenoid valves distributed homogeneously

along the rear part of the model upstream the trailing edges. The pulsating frequency  $F_i$  is selected by a rectangular waveform with duty-cycle of 40 % and is kept constant along the four trailing edges. The system equally enables the user to operate each trailing edge frequency  $F_i$  independently, but connected to the same  $P_i$ . Although the number of solenoid valves is finite, the exit slit with thickness  $h$  of  $(1 \pm 0.1 \text{ mm})$  is continuous and spans all the periphery of the four edges.

Some details of the exit zone where the pulsed jet is generated are shown in figure 3(b). The 32 outlets from the solenoid valves are followed by the circular pipe region (I). All these pipes are equally spaced along the four trailing edges. In this conduit, the flow is convected along  $x$  until arriving at the region (II), where the flow is free to diverge either along  $y$  or  $z$ . The region (II) assumes an important role to obtain an homogeneous outflow. Upstream the exit slit, the flow passes through a sharp elbowed geometry. This might introduce some additional vorticity in the boundary layers of the conduit but an extension of length  $7h$  helps to guide the flow up to the exit section.

Additionally, a Coanda surface can be added just bellow the jet exit as displayed in the same figure. This surface is a quarter of a disk and is installed along the four trailing edges. In the present study, the radius of this geometry is fixed to  $r = 9 \text{ mm}$ , corresponding to 3 % of the model's height. When the Coanda surface is installed,  $\langle C_{p_o} \rangle$  is increased only by 3 % due to a slight flow deviation effect in view of the geometric change (Littlewood & Passmore 2010).

The jet velocity is quantified by a single hot-wire probe 1 mm downstream and at the centerline of the exit slit. An effective jet velocity  $V_{\text{eff}}$  and the momentum coefficient  $C_\mu$  of the jet read:

$$V_{j_{\text{eff}}} = \sqrt{\overline{V_j^2} + (V_{j_{\text{Sdv}}})^2}, \quad (2.3)$$

$$C_\mu = \frac{s_j \overline{V_j^2}}{SU_o^2} = \frac{s_j (V_{j_{\text{eff}}})^2}{SU_o^2}, \quad (2.4)$$

where  $\overline{V_j}$ ,  $V_{j_{\text{Sdv}}}$  and  $s_j$  are the time-averaged jet velocity, its standard deviation and the jet slit cross-sectional area, respectively. Examples of velocity signals for two selected frequencies are reported in figure 4(a).

The effective jet velocity  $V_{j_{\text{eff}}}$  takes into account not only the steady component of the jet velocity but also its oscillatory dynamics. Although the exit slit is 2D due to the designed continuous geometry, the jet velocity presents spanwise variations due to the complex upstream conduits. Measurements of  $V_{j_{\text{eff}}}$  along the edges indicate variations of at most  $\pm 10 \%$  compared to the spanwise averaged velocity. Considering the entire parameter space  $F_i \times P_i$  allowed by our system, the values of  $V_{j_{\text{eff}}}$  are depicted in figure 4(b).

The quantities  $\overline{V_j}$  and  $V_{j_{\text{eff}}}$  are calculated from time-averaging during one pulsation cycle and take into account the time when there is no discharge of fluid from the exit slit. Further details about the pulsed jet formation can be given by the stroke length  $L_o = \int_0^T V_j(t) dt$  as defined in Glezer & Amitay (2002). More specifically, it is possible to show that  $L_o = \overline{V_j} T_i$  with the pulsating period  $T_i = F_i^{-1}$  (Smith & Glezer 1998). As an example,  $L_o = (289 \pm 3)h$  and  $L_o = (14.1 \pm 0.2)h$  for the velocity signals displayed in figure 4(b) respectively when  $F_i = 20 \text{ Hz}$   $F_i = 610 \text{ Hz}$ .

Finally, for spectral analysis, we consider the actuation frequencies in non dimensional form by defining a Strouhal number based on the model's geometry  $St_H = F_i H / U_o$ . The pulsed jet vorticity field  $\omega_z$  during the stroke phase is exemplified in figure 4(c) in the

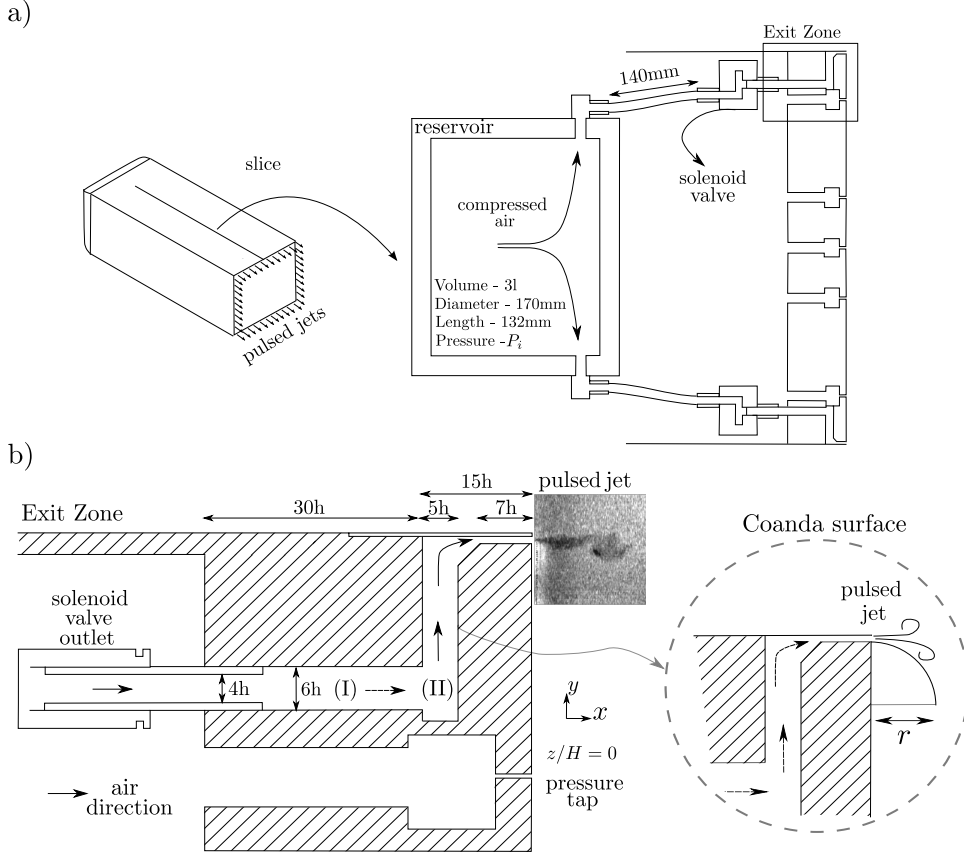


FIGURE 3. Pulsed jet system. a) Sketch of the pulsed jets along the trailing edges and a sectional view through the symmetry plane of the model. The cylindrical plenum chamber (reservoir) as well as its connection to the solenoid valves are displayed. b) Exit zone responsible for the pulsed jet emission. The periodic flow passes through an elbowed conduit until arriving at the exit slit with thickness  $h = 1$  mm. An additional curved surface of radius  $r = 9$  mm can be installed to the setup in order to produce a Coanda effect.

presence or not of the Coanda surface. The actuation parameters are  $St_H = 0.4$  and  $\overline{V}_j = 6.5 \text{ ms}^{-1}$  corresponding to  $L_o = (325 \pm 3)h$ .

### 3. Reference flow

Before analyzing the effects of actuation on the bluff body drag, we briefly review some aspects of its unforced flow. The statistical properties of the recirculating region as well as specific global quantities in the wake are reported. We equally quantify the unsteady shedding mode encountered in this flow.

A general picture of the time mean wake is depicted in figure 5(a), where the streamwise ( $\bar{u}$ ) velocity field at  $Re_H = 3 \times 10^5$  is presented. The momentum deficit in the wake is confirmed by the negative values of  $\bar{u}$ , corresponding to the zone of reverse flow. To give a reference of the recirculating bubble's geometry, the iso-value line  $\bar{u} = 0.25$  is displayed. The recirculating flow length is defined as:

$$L_r = \max(x/H)_{\bar{u}(x/H) \leq 0}, \quad (3.1)$$



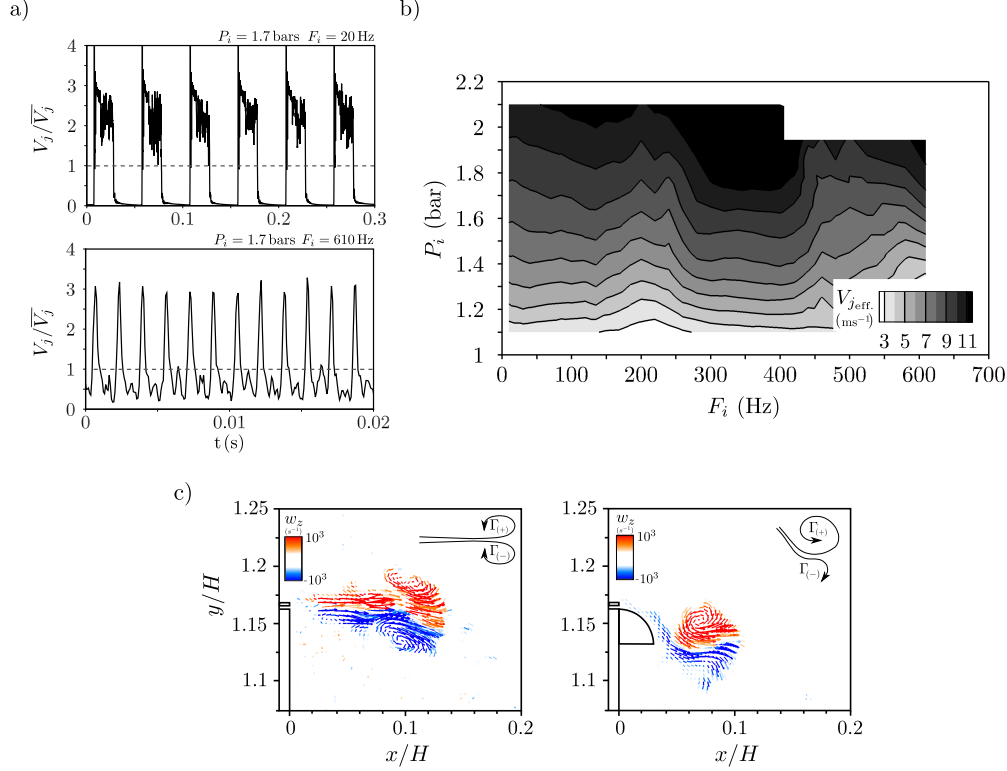


FIGURE 4. Pulsed jet velocity and vorticity field. a) Velocity signals  $V_j$  for two configurations corresponding to an input pressure  $P_i$  of 1.7 bars and frequency  $F_i$  of 20 and 610 Hz. b) Effective jet velocity  $V_{j,eff.}$  on the parameter space  $F_i \times P_i$  for the entire domain of actuation enabled by the setup. c) Vorticity ( $\omega_z$ ) field during the stroke phase of the pulsed jet in quiescent air at an actuation frequency of  $F_i = 20$  Hz corresponding to  $St_H = 0.4$  and  $\bar{V}_j = 6.5$  ms<sup>-1</sup>. The formation of counter rotating vortical structures is indicated by the signs of circulation  $\Gamma$ . The presence of the Coanda surface deviates the pulsed jets.

from which one can estimate the apparent mean bubble size in the streamwise direction. For the present Reynolds number,  $L_r = (1.50 \pm 0.01)$  and agrees with other numerical or experimental studies (Wassen *et al.* 2010; Lahaye *et al.* 2014; Volpe *et al.* 2015).

From the  $\bar{v}$  distribution in figure 5(b), we conclude that the mean wake is dominated by a recirculating motion in the clock-wise direction. Flow asymmetry in the transverse direction is expected due to the presence of the ground, which not only affects the developing boundary layers along the model but also modifies the underflow boundary conditions.

This is particularly clear if we analyze the base pressure partition, as shown in figure 5(c). Close to the upper edge, a low-pressure zone is established where  $(\bar{C}_p)_{min} \sim -0.23$ . It is associated with the large clock-wise recirculating motion which considerably curves the flow streamlines generating high-pressure gradients and a local decrease of pressure. Along the lower edge of the model, the pressure is higher  $(\bar{C}_p)_{max} \sim -0.14$ . Globally, the spatially averaged base pressure is  $\langle \bar{C}_{p_o} \rangle = -0.201$ . It compares well with past values of pressure of this geometry (Krajnovic & Davidson 2003; Grandemange *et al.* 2013).

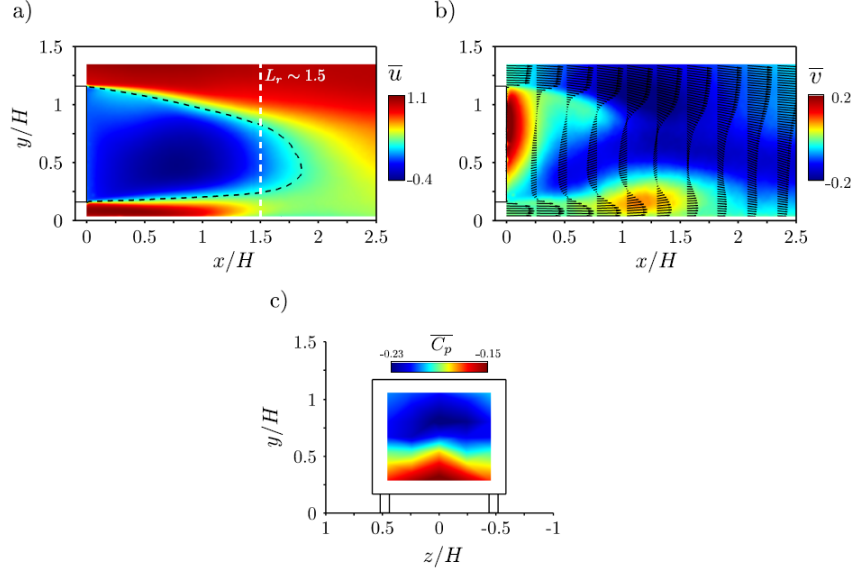


FIGURE 5. Mean properties of the reference wake flow. a) Time-averaged streamwise velocity  $\bar{u}$  with the iso-value line  $\bar{u} = 0.25$ . The recirculating flow length  $L_r$  is displayed by the vertical dashed line. b) Velocity vectors and cross-stream velocity ( $\bar{v}$ ) distribution. c) Base pressure coefficient on the rear surface. The flow corresponds to  $Re_H = 3 \times 10^5$ .

---

Reynolds number - $Re_H$	$L_r$	$\langle \overline{C_{p_o}} \rangle$	$(\overline{C_p})_{\min}$	$(\overline{C_p})_{\max}$	$C_{x_o}$
$2 \cdot 10^5$	$(1.45 \pm 0.01)$	-0.204	-0.240	-0.139	$(0.308 \pm 0.005)$
$3 \cdot 10^5$	$(1.50 \pm 0.01)$	-0.201	-0.233	-0.144	$(0.293 \pm 0.005)$
$4 \cdot 10^5$	$(1.55 \pm 0.01)$	-0.196	-0.219	-0.157	$(0.269 \pm 0.005)$

---

TABLE 1. Recirculation length, base pressure and drag coefficients for varying  $Re_H$  number. The precision on the  $C_p$  values is  $\pm 0.004$ .

---

In table 1, we summarize these quantities for varying Reynolds numbers corresponding to  $U_o = 10, 15$  and  $20 \text{ ms}^{-1}$ , where we additionally include the mean drag coefficient  $C_x$ . There is a decrease of  $C_x$  from 0.31 to about 0.27 when increasing the Reynolds number, with a simultaneous augmentation of  $\langle \overline{C_{p_o}} \rangle$  and  $L_r$ . This tendency has been also observed by other experimentalists (Lahaye *et al.* 2014; Volpe *et al.* 2015) and might be associated to the boundary layer characteristics prior to separation. Indeed, Spohn & Gilliéron (2002) showed the presence of flow detachment on the front curved edges of the model. The perturbations issued from this separation are convected and may impact the separating boundary layer at the rear surface of the model, leading to some modifications on its wake. Besides, an important scatter of the drag values is found in the literature, in which  $C_x$  ranges from 0.25 to up 0.36 (Ahmed *et al.* 1984; Krajnovic & Davidson 2003; Wassen *et al.* 2010; Grandemange *et al.* 2013; Lahaye *et al.* 2014).

Let us quantify now the wake turbulent boundary conditions. For that, we measure the boundary layers prior to separation at the center of each trailing-edge. The streamwise velocity profiles are presented in figure 6, where three locations are chosen: on the upper edge and symmetry plane (A), at the center of a lateral edge (B) and in the under-flow symmetry plane close to the ground (C). Integral and local characteristics of these boundary layers for the different Reynolds numbers are reported in the table 2.

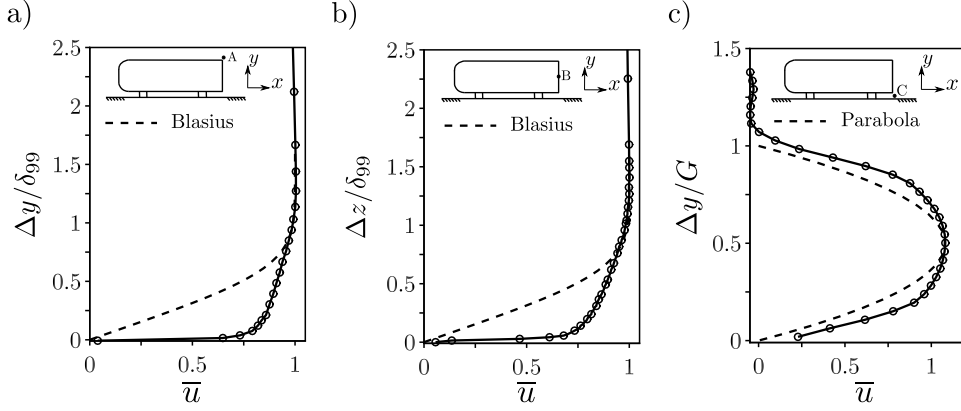


FIGURE 6. Wake turbulent conditions and boundary layer (BL) measurements. BL at the upper (a) and lateral (b) trailing-edges respectively for locations (A) and (B) obtained from HWA. The reference Blasius solution is added for comparison. c) Streamwise velocity profile of the underflow close the ground (C) obtained from PIV. A parabolic profile is added for comparison.

---

$Re_H$	$\delta_{99}$	$\delta^*$	$\theta$	$\bar{H}$	$u_\tau$	$(\overline{u'u'})_{\max}$
$2.10^5(A)$	0.33	0.038	0.030	1.27	0.036	0.011
$3.10^5(A)$	0.22	0.026	0.020	1.33	0.031	0.009
$4.10^5(A)$	0.09	0.014	0.010	1.38	0.027	0.007
$2.10^5(B)$	0.18	0.024	0.015	1.63	0.034	0.009
$3.10^5(B)$	0.12	0.017	0.010	1.70	0.025	0.017
$4.10^5(B)$	0.09	0.014	0.008	1.61	0.022	0.023

---

TABLE 2. Boundary layer characteristics at the trailing-edges A and B.

By comparing to the Blasius and parabolic profiles, the boundary layers clearly carry higher momentum than their laminar analogous. This is confirmed by the calculated shape factor  $\bar{H} = \delta^*/\theta$ , where  $\delta^*$  and  $\theta$  are respectively the displacement and momentum deficit thickness. Their magnitude are considerably lower than the reference value 2.59 obtained from the Blasius solution (Biau 2012). Furthermore, by estimating the friction velocity  $u_\tau$ , the velocity profiles exhibit a log-law behavior which is further detailed in Barros (2015) and not shown here for brevity. The maximum streamwise variance  $(\overline{u'u'})_{\max}$  lies in the range 0.007-0.023.

The separated boundary layers evolve into shear-layer instabilities which grow along the streamwise direction and entrain fluid inside the reverse flow region. The spatial footprint of the shear-layer development is better noticed by the time-averaged velocity fluctuations  $\overline{v'v'}$  and  $\overline{u'v'}$  shown in figure 7. As discussed before, the ground proximity affects considerably the distribution of the cross-stream velocity variance. There is an important concentration of velocity fluctuations along the lower shear-layer issued from the underflow. The streamwise-transverse covariance  $\overline{u'v'}$  better indicates the spatial development of both shear flows up to the closing of the bubble. Extreme values of these quantities together with the streamwise variance  $\overline{u'u'}$  are depicted in the table 3

We additionally report the dimensionless frequency  $f_{n_o} = f_{VS}H/U_o$ , where  $f_{VS}$  is the vortex shedding frequency obtained from HWA spectra. According to Grandemange *et al.* (2013), two oscillatory time-scales  $(f_{n_o})_y$  and  $(f_{n_o})_z$  are associated respectively to the the top/bottom ( $y$ ) and lateral ( $z$ ) interaction of the shear-layers. In the present

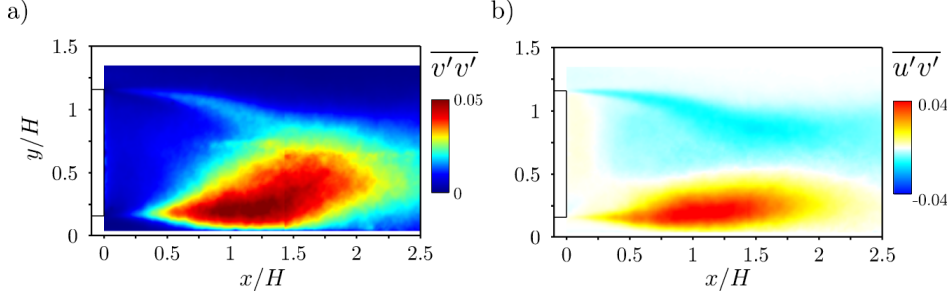


FIGURE 7. Second order statistical moments of the mean flow. a) Cross-stream velocity variance  $\overline{v'v'}$ . b) Streamwise-transverse velocity covariance  $\overline{u'v'}$ .

---

$Re_H$	$(\overline{u'v'})_{\min}$	$(\overline{u'v'})_{\max}$	$\overline{u'u'}$	$\overline{v'v'}$	$(f_{n_o})_y$	$(f_{n_o})_z$
$2.10^5$	-0.016	0.048	0.101	0.055	0.215	0.179
$3.10^5$	-0.015	0.044	0.095	0.053	0.205	0.168
$4.10^5$	-0.017	0.040	0.090	0.047	0.201	0.161

---

TABLE 3. Extreme values of the time-averaged velocity fluctuations and oscillatory wake modes for varying  $Re_H$  number. The precision of the oscillatory mode frequency is  $\pm 0.011$

work, they are measured at two locations: in the symmetry plane of the configuration at  $(x/H, y/H, z/H) = (2.0, 0.9, 0)$  and in a horizontal plane at  $(2.0, 0.6, 0.5)$ . The values of  $(f_{n_o})_y$  are close to 0.2, typically found for axisymmetric bluff bodies (Rigas *et al.* 2014). The lateral shedding values are of the order of 0.17 but, when normalized by  $W$  and not  $H$ , agrees well with the general 0.2 value.

#### 4. Impact of periodic forcing on the drag

Now that we have characterized the actuation system and the natural flow, we will describe the main effects of periodic jet forcing on the baseline pressure and drag. We consider systematic variations of the actuation frequency and amplitude, as well as the influence of the upstream flow velocity. Finally, a summary of the principal results is made to prepare further analysis throughout the manuscript.

##### 4.1. Global effects of actuation

In the following, the base pressure changes represented by the  $\gamma_p$  parameter are quantified. Except otherwise stated, we maintain the same frequency  $St_H$  along all edges and slits. Numerous values of  $C_\mu$  are tested. The global impact of forcing on  $\gamma_p$  is reported in figure 8(a) at a Reynolds number  $Re_H = 3 \times 10^5$ .

For very low frequencies in the range  $St_H \in [0, 0.1]$ , the quasi-steady jet recovers up to 5 % of the base pressure. This is aligned to the past results on active steady control behind square-back geometries, such as the numerical simulations of Roumeas *et al.* (2009) and Wassen *et al.* (2010) as well as the experiments from Krentel *et al.* (2010) and Littlewood & Passmore (2012) with equivalent exit jet velocities  $V_j$ .

An increase of the driving frequency in the range  $St_H \in [0.1, 3.7]$  leads to a noteworthy decrease of base pressure. Two main aspects are remarked in this domain. First, an abrupt augmentation of  $\gamma_p$  at  $St_H \sim 0.4$  decreases up to 25 % the base pressure for  $C_\mu = 5 \times 10^{-3}$ . This Strouhal number is about twice the oscillatory wake mode  $(f_{n_o})_y$  related to the

top/bottom interaction of the shear-layers. The authors relate this phenomena to a vortex synchronization in the recirculating flow caused by actuation (Barros *et al.* 2015). A significant shortening of the wake length is observed, similarly to what has been described on the actuated flow past backward-steps and ramps (Chun & Sung 1996; Dandois *et al.* 2007). Secondly, a broadband range of actuation frequencies increases  $\gamma_p$ . Its maximum amplitude in this domain reaches 1.15 at  $St_H \sim 0.8$  and  $C_\mu = 5 \times 10^{-3}$ . At first glance, there seems to be no relation between this pulsing frequency and another wake instability. Overall, an increase of the jet amplitude  $C_\mu$  correlates to a drop of base pressure close to  $St_H \sim 0.8$ .

A further rise of  $St_H$  beyond 4.0 enables a gradual base pressure recovery. The maximum raise of averaged pressure  $\langle \overline{C_p} \rangle$  is achieved by the highest actuation frequency  $St_H = 12.1$  and equals 16%. The numerical simulations from Dahan *et al.* (2012) carefully illustrated an increase of the step base pressure at high-frequency forcing. Moreover, these results are in agreement with previous tests conducted on axisymmetric wakes (Morrison & Qubain 2009; Oxlade *et al.* 2015).

Corresponding drag measurements are taken at different actuation frequencies and amplitudes. The evolution of the drag parameter  $\gamma_d$  is displayed in figure 8(b). For experimental simplicity, a fixed input pressure is set to  $P_i = 1.45$  bars, leading to several levels of  $C_\mu$  depending on each measured point. As previously noted, this should not disturb our analysis since the effect of  $C_\mu$  on  $\gamma_p$  appears secondary when compared to the actuation frequency  $St_H$  influence.

We notably observe that  $\gamma_d$  is closely connected to the pressure evolution *versus*  $St_H$ . Drag alterations of  $\pm 10\%$  are measured at this Reynolds number. The relation between  $\gamma_d$  and  $\gamma_p$  can be further confirmed by establishing a linear fit in their correlation plot displayed in the inserted picture. The best linear coefficient is 0.68. It reveals that 68% of base pressure changes are converted into drag modifications, in excellent agreement with the findings from the numerical simulations of Krajnovic & Davidson (2003).

#### 4.2. Single edge forcing and Reynolds number dependence

One may hypothesize that these drag changes are linked directly to the shear-layer actuation. To gain further insights on their origin, we select the actuation frequency  $F_i$  for a separated, single edge slit, in order to promote local forcing of individual shear-layers. For that, we call the subscripts  $F_T$ ,  $F_B$ ,  $F_L$  and  $F_R$  respectively the frequencies at the top, bottom, left ( $z > 0$ ) and right ( $z < 0$ ) slits (edges).

Figure 9 presents  $\gamma_p$  *versus*  $St_H$  for a single slit actuation. The effective velocity  $V_{j\text{eff}}$  of each configuration is colored to characterize the forcing amplitude. The two curves corresponding to the lateral forcing ( $F_L$  and  $F_R$ ) collapse and are not repeated to ensure the graph clarity.

A similar qualitative behavior of such curves is recovered when compared to the previous all-slit actuation: an initial increase of  $\gamma_p$  for a broadband range of frequencies followed by the raising of base pressure at higher forcing frequencies. The  $\gamma_p$  values, however, crucially depends on where the actuation is selected. For instance, forcing at the bottom slit ( $F_B$ ) decreases base pressure by at most 3% when  $St_H = 0.8$ , while top ( $F_T$ ) and lateral ( $F_L$ ) actuation promote an increase on  $\gamma_p$  in the range 1.08 – 1.12 at the same driving frequency. An additional feature is the frequency at which the base pressure begins to increase by control when  $\gamma_p = 1$ . Depending on the selected slits, there is a difference of this frequency which lies between  $St_H \in [2.0, 6.0]$ . One would ask if these discrepancies are related to the top/bottom asymmetry due to the ground proximity or to the boundary layer's characteristics. At the present state, we believe that additional measurements are needed to elucidate these facts and should be addressed in future work.

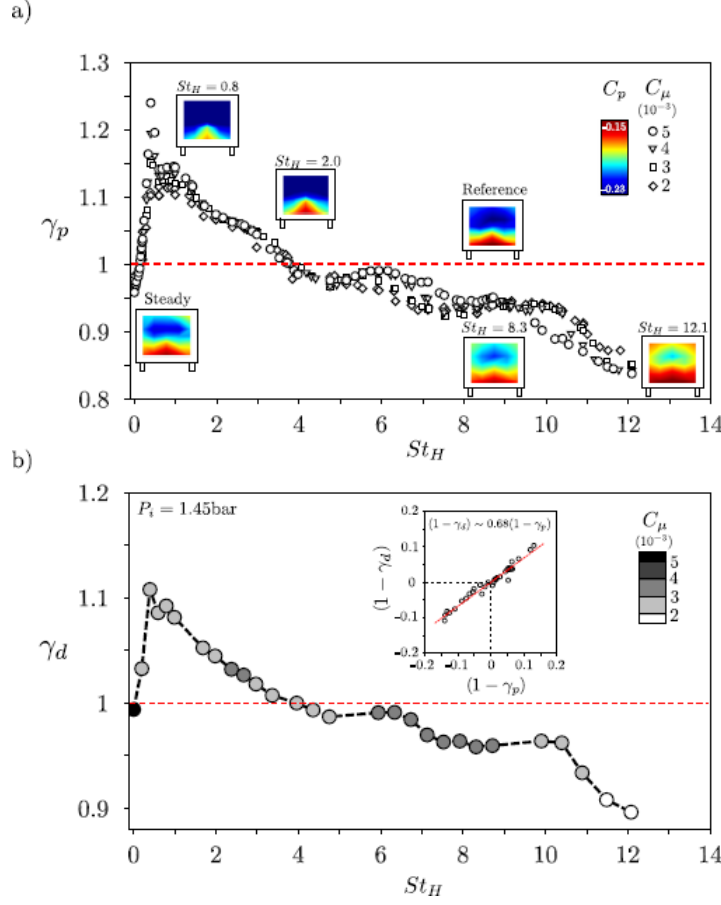


FIGURE 8. Base pressure and drag dependence on the actuation frequency  $St_H$  and momentum coefficient  $C_\mu$ . a) Impact of  $St_H$  and  $C_\mu = \{2, 3, 4, 5\} \times 10^{-3}$  on the base pressure parameter  $\gamma_p$ . The partition of  $C_p$  on the rear surface for representative configurations are shown. b) Drag parameter  $\gamma_p$  modifications for varying actuation frequencies. The measurements are performed at a fixed input pressure  $P_i$  of 1.45 bar. The color bar indicates the corresponding values of momentum coefficient for each measured point of the curve. An inserted correlation plot between  $\gamma_d$  and  $\gamma_p$  indicates that 68% of base pressure changes corresponds to the drag modifications.

Although the magnitude of  $\gamma_p$  is conditioned by the slit selection, the critical frequency remains approximately  $St_H \sim 0.8$ . We may conjecture, *a priori*, that the maximum amplification of  $\gamma_p$  is not necessarily scaled with the boundary layer quantities, given their discrepancies between the four edges as seen in the reference flow. Another two aspects are worthy to remark from these experiments. By comparing the single slit actuation with  $F_{T,B,R,L}$ , detailed in the figure 9, we note that top-slit selection presents control authority in  $St_H \in [0, 4.0]$  given the very similar  $\gamma_p$  values of  $F_{T,B,R,L}$  and  $F_T$ . On the other hand, at high forcing frequencies close to  $St_H \sim 12$ , single slit actuation does not outperform  $F_{T,B,R,L}$ , suggesting that in this range there exists a cumulative effect from all slits when actuated together.

Let us discuss the influence of the Reynolds number on periodic forcing. The effects of  $F_i$  on  $\gamma_p$  at three values of  $Re_H = \{2, 3, 4\} \times 10^5$  are presented in figure 10(a) when actuation is applied along the four edges. First, we note that an increase of the upstream flow velocity  $U_o$  enlarges the broadband range increasing  $\gamma_p$ , consequently augmenting

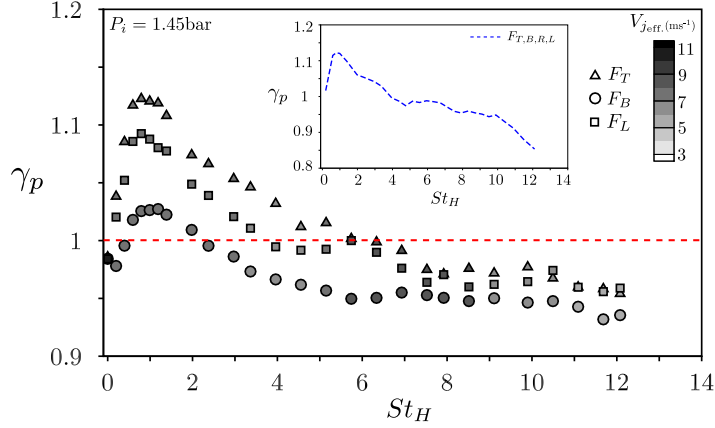


FIGURE 9. Effect of single shear-layer actuation on  $\gamma_p$ . The subscripts T, B and L are related to the forcing at the top, bottom and left ( $z > 0$ ) shear layers. The effective jet velocity  $V_{j\text{eff}}$  is added for the sake of completeness. The inserted plot shows the actuation at all trailing-edges  $F_{T,B,R,L}$ . These measurements are performed with an input pressure  $P_i$  of 1.45 bar at  $Re_H = 3 \times 10^5$ .

the  $F_i$  where  $\gamma_p$  recovers the unity value. For frequencies beyond 400 Hz, there is an almost independence of the  $\gamma_p$  evolution on the Reynolds number, albeit the different magnitudes of base pressure.

A curious point which merits to be emphasized is the role of the momentum coefficient on the forcing conditions. For actuation frequencies close to  $F_i \sim 40$  Hz, only few percent changes of  $\gamma_p$  are measured from varying Reynolds number at the same effective jet velocity  $V_{j\text{eff}} \sim 7.3 \text{ ms}^{-1}$ . Unexpectedly, in despite of  $C_\mu \propto (U_o)^{-2}$ , the variation of  $U_o$  implies very small changes on  $\gamma_p$  indicating that  $U_o$  plays a secondary role at this frequency range. An increase of  $C_\mu$  by augmenting  $V_{j\text{eff}}$ , however, shows a significant effect on  $\gamma_p$  as reported in Barros *et al.* (2015). The injected vorticity from the pulsed jets, together with the actuation frequency, appears to be the governing parameters for this increase of pressure drag. Inversely, at higher actuation frequencies, the upstream velocity is quite relevant to the  $\gamma_p$  modifications and will be further detailed in the following paragraphs.

It is worth to question the importance of the Reynolds number on the single slit actuation, as shown in figure 10(b). A nice collapse of the curves is obtained by normalization using the Strouhal number  $St_H$ . Except for the  $F_B$  actuation, all the other configurations ( $F_{T,B,R,L}$ ,  $F_T$  and  $F_L$ ) exhibit equivalent effects on  $\gamma_p$ . This confirms once more the secondary role of  $C_\mu$  on this wake forcing. As an example, by varying  $F_{T,B,R,L}$  to  $F_T$ , the exit jet area  $s_j$  modifies by a factor of about 4 and so does the  $C_\mu$  value, but the  $\gamma_p$  values remains unchanged.

The maximum value is found at  $St_H \sim 0.8$ , for which the partition of base pressure coefficient is added in detail. Depending on the forced shear-layer, the low-pressure location on the model's base modifies. In general, from the color maps, the actuated side induces the lowest pressure in the rear surface for all tested slits. This change of pressure distribution might be closely related to the dominant recirculating motions inside the wake, a physical problem addressed in § 5.

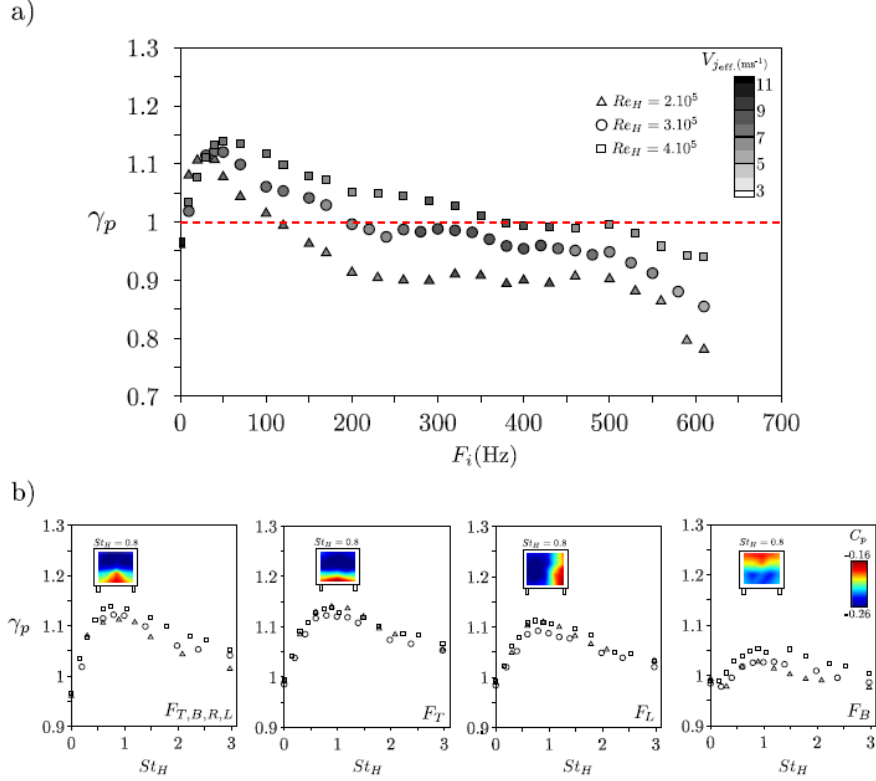


FIGURE 10. Reynolds number effects on the base pressure. a) Dependence of  $\gamma_p$  against the actuation frequency for three different Reynolds numbers  $Re_H = \{2, 3, 4\} \times 10^5$ . The effective jet velocity is added for comparison. b) Effects of the Reynolds number on the broadband low-frequency range for single slit actuation with  $V_{j,eff} \sim 7.3 \text{ ms}^{-1}$ . The base pressure coefficient  $C_p$  when  $St_H \sim 0.8$  is displayed as an example. Similarly to the past graphs, these measurements are performed with an input pressure  $P_i$  of 1.45 bar.

#### 4.3. Summary

From the preceding results, we may conclude that the unsteady, periodic wake manipulation by pulsed jets affects a wide spectrum of time-scales leading to several effects on the model's drag.

By applying quasi-steady forcing, a modest drag reduction of about 1-2% is achieved for the tested jet amplitudes. Actuation at frequencies on the order of the global wake mode  $\mathcal{O}(St_H \sim 0.2)$  results in base pressure decrease, augmenting the drag by at most 10% as evidenced in the present measurements. This frequency range is somehow related to the time-scales of the wake or to its inherent flow instabilities such as the shear-layer amplification or the oscillatory shedding dynamics. On the contrary, higher actuation frequencies leads to a noteworthy decrease of drag of about 10% at  $F_i = \mathcal{O}(60 f_{VS})$ , corresponding to an actuation decoupled to the vortex shedding (VS) instability (Glezer *et al.* 2005).

Within this context, when comparing the present data to past works on periodic shear-flow actuation (Chun & Sung 1996; Dandois *et al.* 2007; Dahan *et al.* 2012; Oxlade *et al.* 2015), we observe many similarities concerning the actuation time-scales and its effects on the wake characteristics such as the recirculating flow or the pressure field inside the



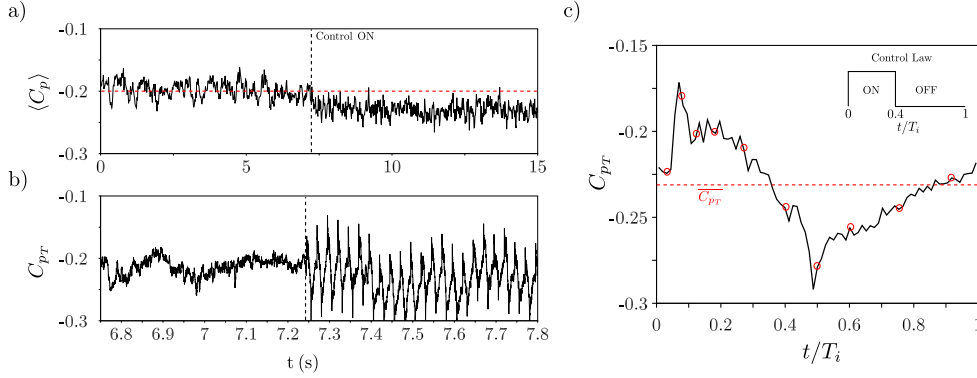


FIGURE 11. Time response of base pressure coefficient for single slit actuation  $F_T$ . The forcing conditions are  $F_T = 40$  Hz ( $St_H = 0.8$ ) and  $V_{j\text{eff.}} \sim 7.3$  ms $^{-1}$ . a) Spatially averaged base pressure coefficient  $\langle C_p \rangle$  transition. The dashed lines represent the  $\langle \overline{C_{p0}} \rangle$  value for the unforced flow. b) Transition to control of the pressure coefficient  $C_{pT}$  located in the symmetry plane of the configuration at  $y/H = 1.05$ , close to the upper trailing edge. c) Phase-averaged pressure coefficient  $C_{pT}$  and control waveform. The circles represent the phases analyzed afterward. The averaged pressure coefficient  $\overline{C_{pT}}$  is indicated by the dashed lines.

bubble. In this sense, we devote the following sections to analyze more deeply the physics of these forced wakes to better understand its impact on the drag changes.

## 5. Increase of drag by low frequency actuation

In order to shed more light into the increase of drag at low frequency actuation, we analyze pressure measurements coupled to the velocity field close to the upper trailing-edge. The Reynolds number is set to  $Re_H = 3 \times 10^5$ . Focus is placed on single slit actuation ( $F_T$ ) at a frequency  $St_H = 0.8$  and with a jet amplitude  $V_{j\text{eff.}} \sim 7.3$  ms $^{-1}$ . This choice is justified by the control authority of the upper slit actuation as well as the simplification of the forcing conditions. Besides, this configuration reduces significantly the base pressure by 12 %, leading to more pronounced changes in the wake flow.

We first show in figure 11(a) the time response of the spatially averaged base pressure when control is turned on, where an overall decrease of  $\langle C_p \rangle$  takes place. Because the forcing is applied along the upper slit, we do not observe the pressure oscillations corresponding to the pulsed jets on the time evolution of  $\langle C_p \rangle$ . Despite of that, by investigating the response of the pressure sensor  $C_{pT}$  located at  $(y/H = 1.05, z = 0)$ , we clearly note in figure 11(b) the periodicity implied by the pulsed jets at the actuation frequency  $F_T = 40$  Hz.

A phase-averaged evolution of the top pressure coefficient  $C_{pT}$  is presented in figure 11(c). The valve opening starts at  $t/T_i = 0$ , as sketched by the rectangular commanded waveform in detail. At the initial stroke phase, a sudden increase of base pressure appears, followed by a gradual decrease of  $C_{pT}$  until the end of the valve opening ( $t/T_i = 0.4$ ). Then, a significant decrease of base pressure is measured ( $t/T_i \sim 0.5$ ) succeeded by a progressive recovery up to the time-averaged value  $\overline{C_{pT}}$  represented by the dashed line.

The interaction of the pulsed jet with the shear layer is better described by the velocity field near the upper trailing-edge. In figure 12, the contour maps of the phase-averaged vorticity field  $\omega_z$  are displayed for selected phases of the actuation cycle indicated in the preceding picture.

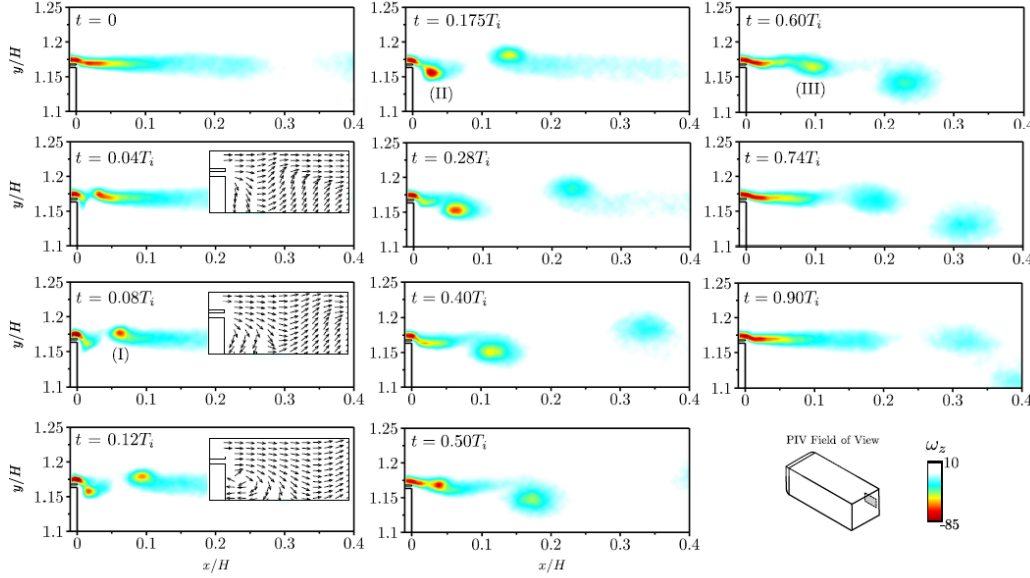


FIGURE 12. Phase-locked vorticity field of the upper shear flow at the forcing frequency  $St_H = 0.8$  and  $V_{j_{\text{eff}}} \sim 7.3 \text{ ms}^{-1}$ . The snapshots correspond to the indicated phases in figure 11(c), respectively  $t = \{0, 0.04, 0.08, 0.12, 0.18, 0.28, 0.40, 0.50, 0.60, 0.74, 0.90\} \times T_i$ . The presence of a detached vortex from the initial disruption of the vorticity sheet (I), the main pulsed vortex head (II) as well as the trailing roll-up (III) can be identified by the vorticity contours maps. Velocity vectors indicating the changes of the velocity field curvature during the formation of (II) are depicted  $t = \{0.04, 0.08, 0.12\}T_i$ .

A first phase-locked snapshot illustrates the vorticity sheet of the separated boundary layer prior to the jet emission  $t/T_i = 0$ . The very beginning of the pulsed jet formation induces a disruption of this vortex layer ( $t = 0.04T_i$ ). It induces the roll-up of a clockwise rotating structure (I) which is convected downstream as remarked when  $t = 0.08T_i$ . At this phase, a noteworthy increase of base pressure is measured, roughly 20 % greater than the time-averaged  $\overline{C_{pT}}$ . An explanation for this sudden pressure raise might be related to the instantaneous change of the velocity field curvature close to the model's edge. Inserted pictures at  $t = \{0.04, 0.08, 0.12\}T_i$  show the wave-like topology of the velocity vectors due to the roll-up of the main vortex head, whose formation is easily evidenced at  $t = 0.175T_i$  (II). This starting vortex is convected at the shear-layer velocity ( $t = 0.28T_i$ ) leading to a drop of  $C_{pT}$ .

A further decrease of pressure is distinguished at the end of the stroke cycle ( $t = 0.40T_i$ ) and immediately after ( $t = 0.50T_i$ ), when a trailing clockwise vortex (III) appears due to the sudden deceleration created by closing the solenoid valve. At this stage ( $t = \{0.60, 0.74\}T_i$ ), both the trailing vortex and the main vortex head are convected and the pressure gradually raises up to  $\overline{C_{pT}}$ .

It is possible to detect a pairing of these structures at about  $t = 0.90T_i$  in view of the higher convective velocity of the trailing vortex. This amalgamation occurs near ( $x/H \sim 0.35$ ) and further details of the process can not be observed with the PIV field of view. Vortex pairing issued from fluidic forcing was also observed in the studies of Chaligné (2013), where base pressure decrease was equally measured.

The dynamics responsible to the base pressure decrease is dominated by the formation

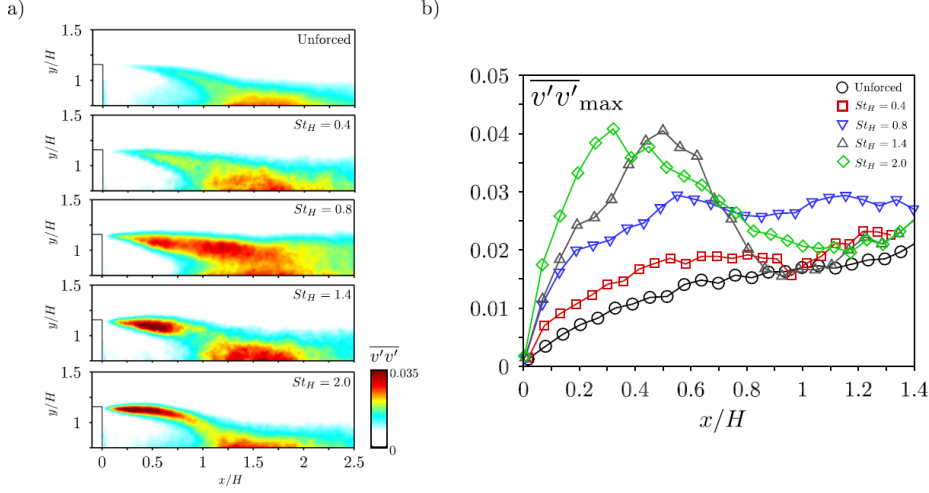


FIGURE 13. Cross-stream velocity variance along the upper shear layer. a) Contour maps of  $\overline{v'v'}$  for several forced configurations  $St_H = \{0.4, 0.8, 1.4, 2.0\}$  at  $V_{j\text{eff.}} \sim 7.3 \text{ ms}^{-1}$ . b) Streamwise evolution of  $\overline{v'v'}_{\max}$  indicating the local enhancement of turbulent fluctuations. The upstream Reynolds number is  $Re_H = 3 \times 10^5$ .

and pairing of vortical structures issued from the pulsed jet forcing, which leads to an enhanced shear-layer mixing and wake entrainment. Although the streamwise evolution of the vortex has not been completely characterized, its main effects are now presented by the statistics of the velocity field of the whole recirculating flow.

Let us analyze the ensemble of velocity snapshots obtained from the large PIV field of view covering the entire near wake flow. For that, we display in figure 13(a) the spatial distribution of the cross-stream velocity variance  $\overline{v'v'}$  along the upper shear-layer separated from the model. The top slit actuation ( $F_T$ ) at the Strouhal numbers  $St_H = \{0.4, 0.8, 1.4, 2.0\}$  and with a forcing amplitude  $V_{j\text{eff.}} \sim 7.3 \text{ ms}^{-1}$  is studied.

An overall increase of velocity fluctuations is noticed for all cases. Recent studies on periodic forcing in mixing layers demonstrated an equivalent increase of turbulent fluctuations, but the forcing conditions and the upstream flow significantly differs from the present study (Parezanović *et al.* 2015). A main feature is a progressive shift of the zones with high  $\overline{v'v'}$  towards the model's edge by the increase of  $St_H$ . This is rather confirmed by the streamwise evolution of  $\overline{v'v'}_{\max}$  shown in figure 13(b). Here,  $\overline{v'v'}_{\max}(x)$  is the maximum value of  $\overline{v'v'}$  along the upper shear-layer. The velocity variance in the forced shear-layers can reach more than twice the values from the unforced flow.

It should be mentioned here that  $\overline{v'v'}$  also increases along the shear layer near the ground, pointing out a connection between the upper and lower shear flows as well as a global enhancement of turbulent fluctuations in the wake. Besides, there exists a correlation between the regions where flow fluctuations are mostly amplified and the drag increase. When the wake is forced at frequencies close to  $St_H \sim 0.8$ , there is an amplification of the shear-layer dynamics along its total streamwise evolution up to the end of the recirculation region at  $x/H \sim 1.5$ . This may explain why the range of frequencies responsible to decrease base pressure is large and not reduced to a discrete time-scale.

One would conjecture that the forcing directly amplify the shear-layer dynamics by its instability mechanisms. Then, we might consider the time scales of the vortical motions linked to this instability in order to compare to our actuation frequency. In figure 14(a),

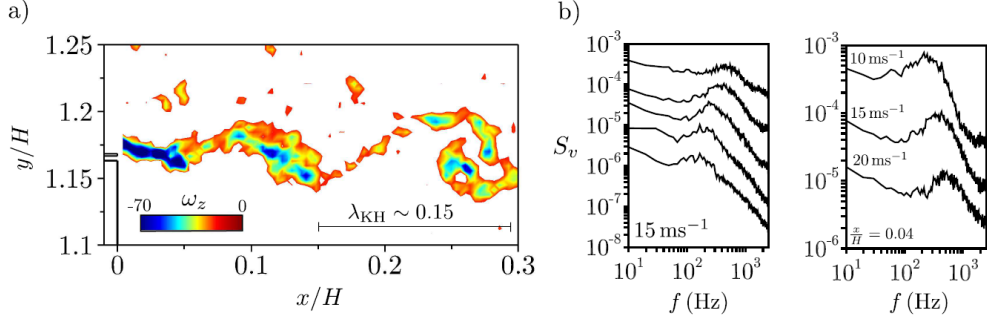


FIGURE 14. Time scales of Kelvin-Helmholtz (KH) instabilities in the unforced flow. a) Vorticity snapshot of the initial roll-up along the upper shear layer and KH length scale  $\lambda_{KH}$  ( $U_o = 15 \text{ ms}^{-1}$ ). b) Left: power spectral density  $S_v$  of the cross-stream velocity  $v$  at the streamwise positions  $x/H = \{0.02, 0.04, 0.08, 0.185, 0.27\}$  (from top to bottom) when  $U_o = 15 \text{ ms}^{-1}$ . Right:  $S_v$  at  $x/H = 0.04$  for varying upstream velocity  $U_o = 10, 15, 20 \text{ ms}^{-1}$ .

a vorticity snapshot of the unforced flow when  $U_o = 15 \text{ ms}^{-1}$  indicates the presence of coherent Kelvin-Helmholtz (KH) roll-up in the vicinity of the upper edge.

Power spectral density  $S_v$  of the velocity signals at several streamwise locations  $x/H = \{0.02, 0.04, 0.08, 0.185, 0.27\}$  is computed and displayed in figure 14(b, left). At each streamwise position, a broadband range of frequencies is remarked. Moreover, the value of the most amplified frequencies decreases along  $x$ , in agreement with the well-known shear-layer growth (Ho & Huerre 1984).

By normalizing them with the wake time scale  $f_H = \frac{fH}{U_o}$ , the maximum measured peaks are  $f_H = \{9.7, 7.6, 4.8, 3.8, 3.2\}$  respectively for the increasing values of  $x$ . Generally, they correspond to frequencies one order of magnitude higher than the vortex shedding mode (Prasad & Williamson 1997). This behavior is also found when we vary the upstream velocity  $U_o$ , as shown by the plot of  $S_v$  measured close to the edge ( $x/H = 0.04$ ) in figure 14(b, right).

If we use now the dimensionless frequency  $f_{\delta\omega_z} = f\delta\omega_z / (0.5U_o)$  for the initial instability at  $x/H = 0.04$ ,  $f_{\delta\omega_z} = \{0.23, 0.25, 0.29\}$  respectively for  $U_o = 10, 15, 20 \text{ ms}^{-1}$ . These values are in agreement with the mixing layer characteristics measured by Bonnet *et al.* (1998) but much controversy exists concerning the correct length scale for the KH mode in turbulent shear-layers (Morris & Foss 2003).

Interestingly, the length scale  $\lambda_{KH} \sim 0.15$  detailed in figure 14(a) represents a frequency of about  $f_{KH} \sim 0.5U_o\lambda_{KH}^{-1} \sim 168 \text{ Hz}$ , scaling well with the  $f_H = 3.2$  value obtained at  $x/H = 0.27$ . Hence, the KH roll-up process is related to the amplified frequencies further downstream the edge ( $x/H \sim 0.27$ ) and not at the initial instability  $x = 0$ .

We compare now our low-frequency forcing frequency with this most amplified KH mode. When  $St_H = 0.8$ , the frequency  $F_i = 40 \text{ Hz}$  is approximately one-fourth of  $f_{KH}$ : albeit they are of the same order, this highest increase of drag is not linked to the KH roll-up at first analysis.

There is an evident interaction between our pulsed jet forcing and the shear instabilities. Yet, given the amplitude of actuation and its phase-averaged evolution, it appears that the jet dynamics dominates the shear-layer surrounding the recirculating flow. Specifically in the present problem, our results suggest that the concepts of low actuation is more related to the convection of the periodic jet structures responsible to enhance mixing and increasing the cross-stream shear-layer dynamics.

Previous studies have shown a close link between the augmentation of cross-stream

velocity variance and a raise of drag (Parezanović & Cadot 2012; Raspa *et al.* 2013). When considering a local analysis, we confirm the influence of  $\overline{v'v'}$  on the base pressure by writing the time-averaged  $y$  momentum equation:

$$\frac{\partial \bar{p}}{\partial y} = -\rho \left( \bar{u} \frac{\partial \bar{v}}{\partial x} + \bar{v} \frac{\partial \bar{v}}{\partial y} + \frac{\partial \overline{u'v'}}{\partial x} + \frac{\partial \overline{v'v'}}{\partial y} \right). \quad (5.1)$$

The pressure gradient across the wake explicitly depends on the  $\overline{v'v'}$  gradient, which, when integrated, leads to a drop of local pressure not only along the shear-layers but also in the whole wake, when amplification of  $\overline{v'v'}$  is observed up to the end of the recirculating region (figure 13(a)) for  $St_H = 0.8$ .

Globally, the modifications of the turbulent dynamics along the shear-layer importantly impact the entrained flow inside the wake. According to Gerrard (1966), the characteristics of the shear layers in the vicinity of the recirculating bubble end are relevant to the wake formation. Motivated by the entrainment scenario proposed in his work, we study the distribution of the time-averaged cross-stream velocity  $\bar{v}$ . For that, we analyze the mean velocity field when the actuation frequency is  $St_H \sim 0.8$ , leading to the highest augmentation of drag and cross-stream velocities. More specifically, we identify the regions where  $|\bar{v}|$  is maximum, as displayed in figure 15.

In figure 15(a), three domains corresponding to the higher  $\bar{v}$  velocities are illustrated. Region (I) indicates the upward flow adjacent to the rear surface where  $\bar{v}$  is greater than 0.06. There is an increase of  $\bar{v}$  when actuation is applied, attested quantitatively by a velocity profile at  $x/H = 0.05$  as shown in figure 15(b, left). At least when considering this symmetry plane data, it strongly suggests that more fluid is entering in the wake.

We confirm that by analyzing the cross-stream flow entrained at the end of the recirculating bubble in the regions (II) and (III). They respectively indicate the highest downward ( $\bar{v} < -0.2$ ) and upward ( $\bar{v} > 0.06$ ) velocities in the wake. While the upward motion in region (III) shows modest changes, a significant increase of downward flow is noted in region (II), better confirmed by the velocity profiles shown in figure 15(b, right) at the streamwise location  $x/H = 1.1$ . Besides, in the forced wake, both regions are displaced upstream revealing a shortened deadwater region.

The flow topology is represented in figure 15(c) by the streamlines of the mean velocity field in the symmetry plane. This is of course a qualitative 2D picture of the bubble geometry and we remark these traces are not the real streamlines of the flow. The dominating clockwise recirculating motion is clear from the pictures. Both the reference and the forced wake present the same features, but a decrease of 11% on the bubble's length  $L_r$  is measured for the actuated flow.

The mixing enhancement along the shear-layers promoted by periodic forcing induces higher entrained flow inside the wake and reducing the bubble region. A physical measure of the entrained reverse flow is now quantified by evaluating the integral of  $|\bar{v}|$  and the total kinetic energy along  $y$  and inside the domain  $\Omega_{\bar{u} < 0}$  as:

$$\mathcal{V}_+(x) = \int_{\Omega_{\{\bar{u} < 0\}}} |\bar{v}(x, y)| dy, \quad (5.2)$$

$$\mathcal{E}(x) = \int_{\Omega_{\{\bar{u} < 0\}}} \left( \frac{\bar{u}^2 + \bar{v}^2 + \overline{u'u'} + \overline{v'v'}}{2} \right) dy. \quad (5.3)$$

As shown in figure 15(d), an increase of both quantities is perceived in the forced wake. Not only a more intense cross-stream dynamics is measured by the streamwise evolution of  $\mathcal{V}_+$  but also an enhancement of the reverse flow kinetic energy is measured by an

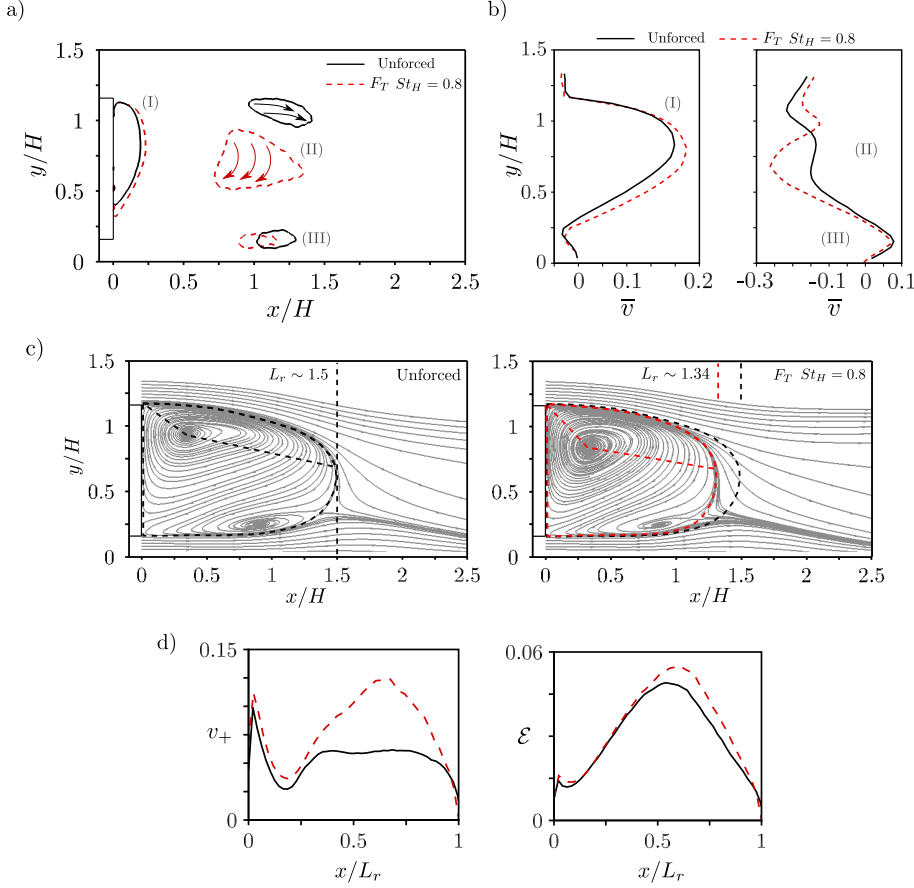


FIGURE 15. Global effects of actuation ( $St_H = 0.8$ ,  $V_{j_{\text{eff}}} \sim 7.3 \text{ ms}^{-1}$ ) on the time-averaged wake. a) Domains of intense cross-stream velocities  $\bar{v}$ : regions (I) and (III) are the contour lines inside which  $\bar{v} > 0.06$ , and region (II) are contour lines limiting the zones where  $\bar{v} < -0.2$ ; full and dashed lines correspond respectively to the unforced and forced wakes. b) Velocity  $\bar{v}$  profiles across the regions at the streamwise locations  $x/H = 0.05$  and  $x/H = 1.1$ . c) Modifications of the recirculating bubble topology and stream traces, indicating the reduction of the length  $L_r$ . d) Evolution of  $v_+$  and  $\mathcal{E}$  (see text) in the reverse flow.

augmentation of  $\mathcal{E}$ . This scenario is in agreement to the conceptual model proposed by Gerrard (1966) and correlates the shortening of the bubble region to the amount of the entrained flow governing the formation region.

The equilibrium of the forced recirculating flow shows a smaller bubble length and higher entrained fluid in the wake. It is natural to deduce that a decrease of the bubble size, with the conservation of its shape, leads to an adjustment of the velocity field curvature. The aspect ratio of the bubble  $L_r/H$  has been decreased by the forcing, increasing the wake bluffness. Although it is an intuitive concept, as remarked in the seminal paper Roshko (1955), one may conclude that a change of the aspect ratio of the bubble might be associated to the balance of equilibrium forces along its boundary Roshko (1993a). Results from the thesis of Parezanovic (2011) shows a good correlation between the bubble's aspect ratio and the model's base pressure in 2D wakes.

Recalling the streamwise momentum balance first used by Sychev (1982) and revisited by Roshko (1993a,b) and Balachandar *et al.* (1997), we write the equilibrium of the forces

acting along the closing separating line of the bubble in an analogy to the simplified two-dimensional wake:

$$\langle C_{p_b} \rangle H = \int_{\partial \mathcal{B}} C_p (\vec{n} \cdot \vec{x}) ds + 2 \int_{\partial \mathcal{B}} \overline{u'u'} (\vec{n} \cdot \vec{x}) ds + 2 \int_{\partial \mathcal{B}} \overline{u'v'} (\vec{n} \cdot \vec{y}) ds, \quad (5.4)$$

where  $\vec{x}$  and  $\vec{y}$  are the normal vectors of the reference system,  $\vec{n}$  the vector normal to the differential  $ds$  of the bubble boundary  $\partial \mathcal{B}$ . Fluxes of mean momentum across the wake boundary are assumed negligible.

As discussed in Balachandar *et al.* (1997), the normal and shear contributions of the right-hand side of the equation are both significant for the wake equilibrium, their magnitude varying more or less depending on the bluff body and wake characteristics. When forcing is applied, a variation of the model's base pressure would obey  $\delta \langle C_{p_b} \rangle \sim \delta \langle C_{p_{\partial \mathcal{B}}}, \overline{u'u'}, \overline{u'v'} \rangle$ . The contribution from the normal Reynolds stress  $\overline{u'u'}$  is positive as  $\vec{n} \cdot \vec{x} > 0$ . On the contrary,  $\vec{n} \cdot \vec{y}$  may be positive or negative and the  $\overline{u'v'}$  term leads to a negative contribution to  $\langle C_{p_b} \rangle$ . An increase of deviated momentum across the bubble from the external flow by an amplification of  $\overline{u'v'}$  would decrease the base pressure.

In order to get a picture of this balance in our study, we report in figure 16(a) the evolution of the Reynolds stresses along the bubble boundary  $\partial \mathcal{B}$  following the path  $s$ , starting from the upper shear layer at  $s_o$  (see detail in the picture). Few variations concerning the normal streamwise stress  $\overline{u'u'}$  are measured. A slight increase due to the upper shear-layer forcing is verified followed by a modest drop of its value. Concerning the shear-stress  $\overline{u'v'}$ , there is a clearer augmentation of its magnitude at the beginning of the upper layer as well as from  $x/H > 0.5$  along the bottom shear-layer. The highest raising comes for the cross-stream variance  $\overline{v'v'}$ , where a significant increase is measured along the whole boundary. These tendencies are robust inside the wake, as suggested by figure 16(b) where the Reynolds stresses are integrated inside a rectangular region  $\mathcal{R}$  limited by the body height up to  $x/H = 1.5$ .

There are no significant changes of the Reynolds stresses playing at equation 5.4. Even though our flow is fully 3D and we have not taken into account the terms along the  $z$  direction, it appears that a balance from  $\overline{u'u'}$  and  $\overline{u'v'}$  would be established, qualitatively leading, at first order, to  $\delta \langle C_{p_b} \rangle \sim \delta \langle C_{p_{\partial \mathcal{B}}} \rangle$ . One would question about the influence of  $\overline{v'v'}$  on  $\delta \langle C_{p_b} \rangle$ , given its importance on the flow dynamics. We may conjecture the enhancement of  $\overline{v'v'}$  along the wake implicitly affects this wake equilibrium. By our previous analysis from equation 5.1,  $\overline{v'v'}$  plays a direct role in establishing the  $C_p$  along  $\partial \mathcal{B}$  by modifying the velocity field curvature and pressure gradients. Then, in the time-averaged sense, the pressure values on the recirculating flow boundary are dependent on the cross-stream velocity variance.

In this section, we explored how the periodic forcing affects the shear-layer and wake dynamics. By a complex vortex dynamics generated from the formation and convection of the pulsed jets, large-scale eddies entrain fluid inside the wake by engulfment process (Philip & Marusic 2012), resulting in a shortened recirculating flow. To a further proof of the additional entrainment along the shear flow, we force the opposite (bottom) shear layer at the same Strouhal number  $St_H = 0.8$ . There is a huge change the main recirculating motion, as illustrated by the contour maps of the time-averaged cross-stream velocity  $\bar{v}$  in figure 17. The rotation sense inside the wake is inverted and correlates to the local pressure drop on the bottom of the model's rear surface as previously shown in figure 10(b). The additional large-scale eddies along the bottom shear layer compensates

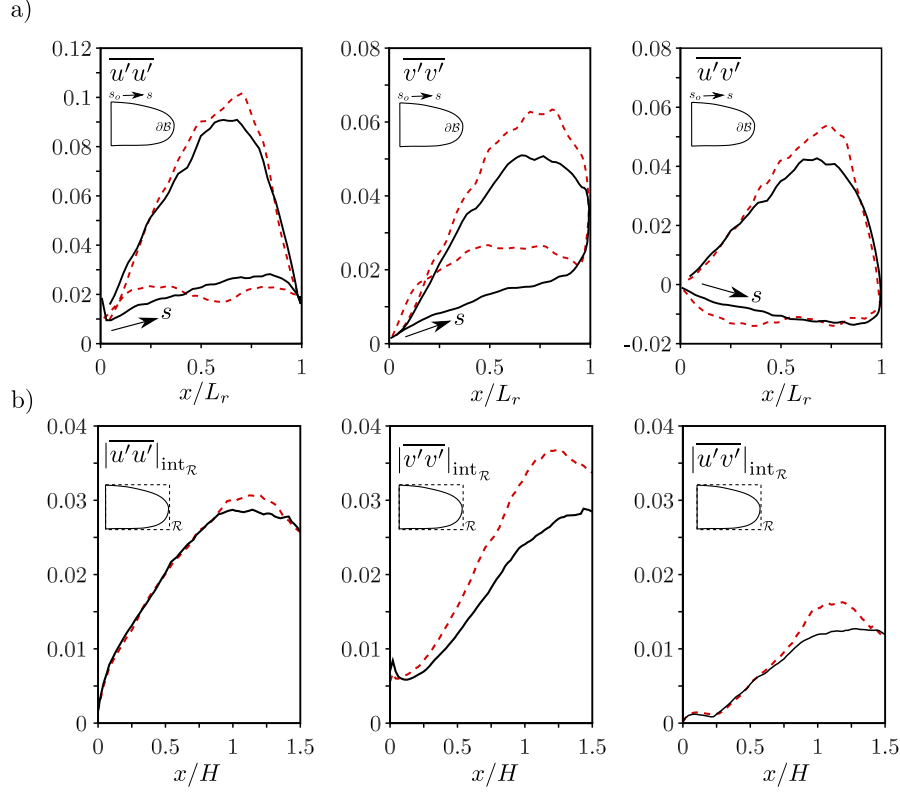


FIGURE 16. Reynolds stresses along on the bubble. a) Evolution of  $\overline{u'u'}$ ,  $\overline{v'v'}$  and  $\overline{u'v'}$  along the bubble boundary  $\mathcal{B}$  starting from the  $s_o$  position on the upper shear-layer. b) Cross-stream integral of the Reynolds stresses inside rectangular region  $\mathcal{R}$  limited by the height of the model up to  $x/H = 1.5$ . The dashed lines correspond to the forcing at  $St_H = 0.8$  and  $V_{j_{\text{eff}}} \sim 7.3 \text{ ms}^{-1}$ .

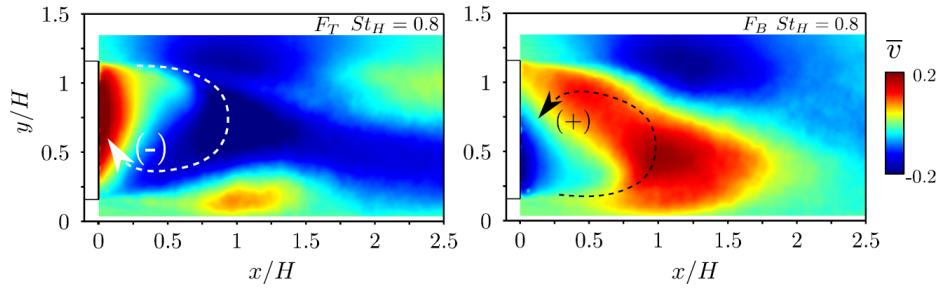


FIGURE 17. Inversion of the recirculating flow as a consequence of actuation at  $St_H = 0.8$  on the lower shear-layer. The time-averaged cross-stream velocity field  $\bar{v}$  is depicted for both configurations.

the entrained fluid of the opposite edge, leading to stronger engulfing motions closer to the ground and a consequent reorientation of the deadwater recirculation.



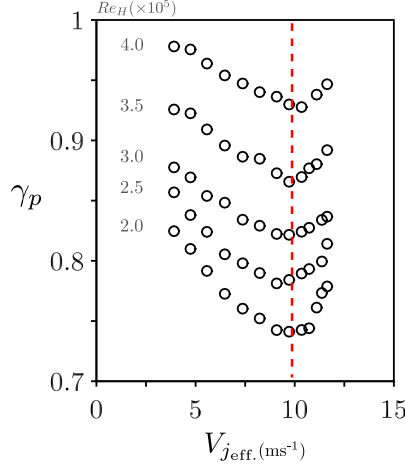


FIGURE 18. Effects of upstream flow velocity  $U_o$  and pulsed jet velocity  $V_{j_{\text{eff}}}$  on the base pressure recovery at the actuation frequency  $St_H = 12.1$  on all slits. The studied Reynolds numbers  $Re_H = \{2.0, 2.5, 3.0, 3.5, 4.0\} \times 10^5$  are indicated in the graph and correspond respectively to  $U_o = \{10, 12.5, 15, 17.5, 20\} \text{ ms}^{-1}$ . The vertical dashed line indicates the optimum value  $V_{j_{\text{eff}}} \sim 9.1 \text{ ms}^{-1}$  measured for all upstream conditions.

## 6. Decrease of drag by high frequency actuation

Following the results of § 4, actuation at high frequencies increases the baseline pressure resulting in drag reductions of the order of 10 % in the tested range of jet parameters. Furthermore, a decrease of the pulsing time scale shifts the shear-layer mixing closer to the model's edge. Here, we attempt to distill the physical mechanisms leading to both effects by addressing two questions: how do the flow changes by high frequency actuation impact the base pressure? and how does it depend on the upstream flow and jet amplitude? We are mainly concerned with these mechanisms to further propose a conceptual scenario of actuation at this time scale.

### 6.1. Overview of the main effects

It was generally confirmed in § 4 the dependence of  $\gamma_p$  on  $C_\mu$  by varying either the jet amplitude or the Reynolds number. In figure 18, these features are represented from systematic changes of  $V_{j_{\text{eff}}}$  for several upstream flow velocities  $U_o$  at an actuation frequency  $St_H = 12.1$  ( $F_{T,B,R,L}$ ), corresponding to the best drag reduction previously discussed.

The effect of these quantities is clear: the base pressure parameter decreases monotonically as  $U_o$  and with the increase of  $V_{j_{\text{eff}}}$  up to a critical value, where a minimum of  $\gamma_p$  appears. This optimality has been equally found in the forced wake past an axisymmetric geometry (Oxlade *et al.* 2015). In our case, it is observed at the same  $V_{j_{\text{eff}}} \sim 9.1 \text{ ms}^{-1}$  for all studied upstream flows  $U_o = \{10, 12.5, 15, 17.5, 20\} \text{ ms}^{-1}$  leading to an increase of base pressure by 7, 13, 18, 22 and 26 % for decreasing values of  $U_o$ . Once more, similarly to the low frequency actuation, the results suggest that the dimensionless  $C_\mu$  does not govern the jet amplitude effect at high frequency forcing given the same optimal  $V_{j_{\text{eff}}}$  at different upstream velocities.

As commented in § 5, a sudden increase of local pressure at the very beginning of the low frequency actuation cycle at  $St_H = 0.8$  ( $F_T$ ) takes place. This has been related to the initial formation of the main vortex head locally deviating the velocity field and altering its curvature properties, as illustrated in figure 12. One would ask if this mechanism

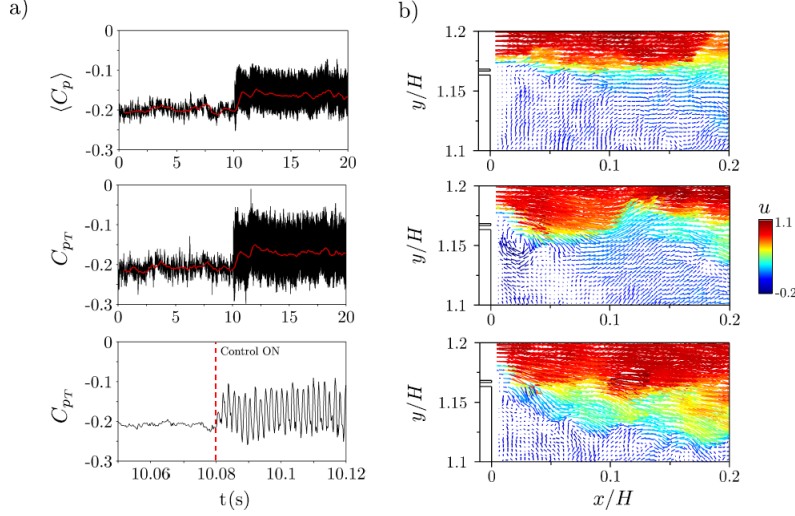


FIGURE 19. Base pressure time response and shear-layer flow during transition to control applied at  $St_H = 12.1$ ,  $V_{j\text{eff.}} \sim 9.1 \text{ ms}^{-1}$  and  $Re_H = 3 \times 10^5$ . a) Response of the averaged base pressure  $\langle C_p \rangle$  (top) and the pressure coefficient  $C_{pT}$  (middle and bottom). b) Velocity field snapshots: unforced flow prior to actuation (top), actuation cycle (middle) and shear layer vectoring (bottom). The vectors are colored by the streamwise velocity  $u$ .

happens at high driving frequencies given the intense flow activity generated close to the edge due to the pulsing time scale reduction.

In order to confirm that, we proceed analogously to the low-frequency case by investigating the transient response when actuation at  $St_H = 12.1$  is applied with the optimum jet amplitude when  $U_o = 15 \text{ ms}^{-1}$ . Figure 19(a) shows that the start of control suddenly increases  $\langle C_p \rangle$  as well as the top pressure coefficient  $C_{pT}$ , as indicated by their filtered evolution represented by the red lines. A magnified view in the bottom figure enables us to observe with more details the pressure oscillations resulting from the pulsed jet frequency. The pressure magnitude alternates between the unforced and higher values, leading to a time-averaged increase of  $\langle C_p \rangle$  of 18 %.

Figure 19(b) displays three snapshots of the velocity field during this transition. The unforced shear-layer prior to actuation is depicted in the top. By starting the control, we observe the formation of a circulatory flow (middle) very close to the edge, similar to what has been measured at the beginning of the stroke cycle at lower actuation frequencies. This injected circulation induces a notable deviation of the shear layer. It reminds the flow vectorization by adjacent synthetic-jet control reported in Smith & Glezer (2002).

In figure 20, we quantify this process by computing the circulation and the cross-stream velocity at specific regions of interest. By integrating the vorticity field inside a rectangular region  $\Omega$  adjacent to the exit slit very close to the rear surface and limited by  $(x/H, y/H) = ([0, 0.03], [1.14, 1.17])$ , we observe in figure 20(a) an increase of flow circulation  $\langle \Gamma \rangle_\Omega$  inside this domain, in agreement to the previous snapshot illustrating the circulatory motion there. The accumulation of  $\langle \Gamma \rangle_\Omega$  induces a downward flow responsible to deviate the shear-layer, as shown in figure 20(b) where the cross-stream velocity  $\langle v \rangle_\Omega$  is computed from integration inside an extended domain  $\Omega$  limited by  $(x/H, y/H) = ([0, 0.07], [1.15, 1.19])$ . When the actuation is started, the downward cross-stream velocity significantly raises to values of about 8 % of  $U_o$ . The fluctuations of both  $\langle \Gamma \rangle_\Omega$  and  $\langle v \rangle_\Omega$  indicate that the shear-layer flaps due to the high-frequency injection of circulation leading to the observed oscillations on  $C_{pT}$ .

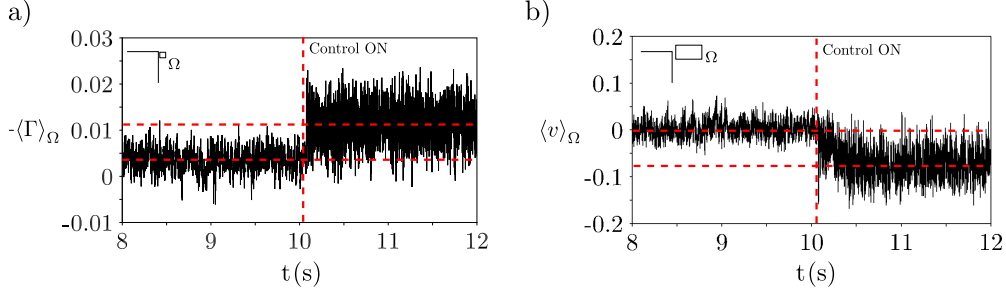


FIGURE 20. Effects of forcing on the shear layer deviation at  $U_o = 15 \text{ ms}^{-1}$ . a) Circulation  $\langle \Gamma \rangle_\Omega$  in the domain  $\Omega$  limited by  $(x/H, y/H) = ([0, 0.03], [1.14, 1.17])$  adjacent to the exit jet slit. b) Time response of the integrated velocity  $\langle v \rangle_\Omega$  over the rectangular domain  $\Omega$  limited by  $(x/H, y/H) = ([0, 0.07], [1.15, 1.19])$ .

Due to the resolution of our PIV velocity field, we are not capable to spatially resolve the main pulsed vortex head at this actuation frequency, whose length scale is of the order of the actuation slit ( $\sim 1 \text{ mm}$ ). Yet, flow visualizations acquired using this setup shed some light in the phenomenology of this forcing, as illustrated in figure 21.

Two counter-rotating vortex emerge from the exit slit at the beginning of the actuation cycle. This started jet structure is quite similar to the Schlieren visualizations of synthetic jets during the stroke phase by Smith & Glezer (2005). Its averaged diameter is of the order of the slit thickness  $h \sim 1 \text{ mm}$ . As the adjacent flow close to each structure is different (boundary layer at one side and recirculating flow just below the jet), the clockwise rotating vortex with carrying negative vorticity remains close to the edge while the upper structure is convected with about  $V_c \sim 0.5U_o$ . Interestingly, at the beginning of the forthcoming actuation period ( $t + T_i$ ), the new pulsed jet interacts with the preceding clockwise vorticity, resulting in a merged structure which is convected along the shear-layer.

Power spectral density ( $S_v$ ) of the cross-stream velocity at  $(x/H, y/H) = (0.03, 1.16)$  proves the existence of vortex amalgamation by the presence of the first subharmonic of the actuation frequency  $F_i$  corresponding to  $St_H = 12.1$  (see detail in the figure). Similarly, the new clockwise vortex still remains close to the edge and is convected until the end of the period. In the following cycle ( $t + 2T_i$ ), however, there is no interaction between the structures. This vortex dynamics leads to a periodic accumulation of circulation close to model edges, leading to shear-layer deviation towards the center of the separated flow.

The resulting time-averaged shear-layer is illustrated by the velocity streamlines together with its cross-stream  $\bar{v}$  field in figures 22(a). There is an overall increase of the downward velocity magnitude, clearly noted by the flow streamlines. Interestingly, the region of upward flow adjacent to the body surface (indicated by red color in the maps) is significantly reduced, suggesting reduction of both local entrainment along the shear-layers and large-scale engulfment at the end of the bubble region.

In figure 22(b), we compute the velocity angle  $\beta$  along the separating stream traces originated at  $(x/H, y/H) = (0, 1.17)$ . First, the reference flow presents low velocity deviation close to the edge and the streamlines are slightly directed downwards. Minimum velocity angles of  $-4^\circ$  are calculated at about  $x/H \sim 0.3$ . On the other hand, the forcing importantly deviates the flow at the very beginning of the shear-layer with angles of  $-10^\circ$  which gradually decreases along  $x$ . From the streamwise evolution of the forced case, we can deduce that significant changes of the velocity field curvature takes place, modify-

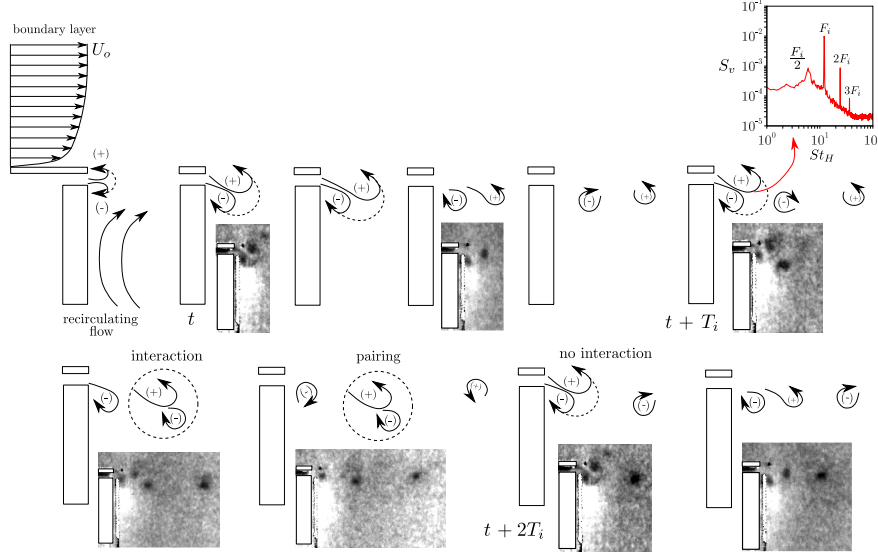


FIGURE 21. Phenomenology of the pulsed jet formation at high frequency forcing  $St_H = 12.1$ . The picture shows the vortex formation and its interactions along two actuation cycles. The power spectral density  $S_v$  of the cross-stream velocity at  $(x/H, y/H) = (0.03, 1.16)$  evidences the apparition of vortex merging which is visualized by the corresponding pictures.

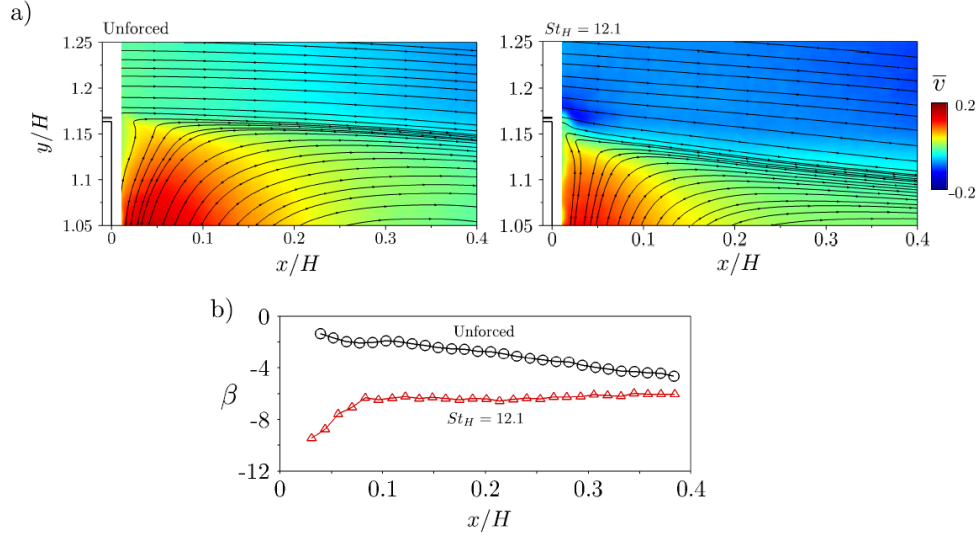


FIGURE 22. Stream traces and time-averaged cross-stream velocity  $\bar{v}$  distribution. The actuation parameters are  $St_H = 12.1$  and  $V_{j,eff.} \sim 9.1 \text{ ms}^{-1}$ . Separating streamlines are represented by dashed lines emanated from the top edge of the model in the symmetry plane. c) Velocity angle  $\beta$  along the corresponding streamlines for both unforced and forced wakes.

ing the pressure gradients across the shear-layer. As an analogy to the passive control discussed in § 1, this time mean scenario indicates a *fluidic boat-tailing* effect where the pulsating jets deviate flow without geometric modifications leading to a base pressure recovery and drag reduction.

### 6.2. Influence of the jet amplitude

The intensity of flow deviation by the produced circulation flux close to the model must be somehow related to the jet amplitude. We investigate it by comparing the effects of the optimal  $V_{j\text{eff.}} \sim 9.1 \text{ ms}^{-1}$  to a smaller amplitude  $V_{j\text{eff.}} \sim 5.6 \text{ ms}^{-1}$  corresponding to input pressures  $P_i$  of 1.65 and 1.45 bar respectively. Profiles of the  $\bar{v}$  velocity, the vorticity  $\omega_z$  and the cross-stream fluctuations  $\overline{v'v'}$  are reported in figure 23. They are measured at two streamwise positions along the upper shear layer ( $x/H = \{0.1, 0.3\}$ ) at a Reynolds number  $Re_H = 3.0 \times 10^5$ .

The shear-layer vectoring is noticed for both cases by analyzing the decrease of  $\bar{v}$  at the first streamwise location  $x/H = 0.1$ . A decrease of flow deviation is associated to the smaller jet amplitude. On the other hand, an increase of  $V_{j\text{eff.}}$  to  $11.6 \text{ ms}^{-1}$  (not shown here for brevity) does not further deviate the flow, in agreement to the optimality of  $V_{j\text{eff.}} \sim 9.1 \text{ ms}^{-1}$ . Further downstream at  $x/H = 0.3$ , the profiles are quite similar for both jet amplitudes.

Additionally to the flow deviation, a drop of the minimum time-averaged spanwise vorticity  $\omega_z$  is measured. This is accompanied by an enlargement of the vorticity thickness and the produced effect is higher for the optimal jet velocity. A decrease of the vorticity peak and the enlargement of the initial shear-layer thickness modify its stability properties and streamwise growth (Ho & Huerre 1984). These aspects are quantified later.

Finally, there is an expected increase of  $\overline{v'v'}$  at  $x/H = 0.1$  due to the pulsed jet dynamics close to the slit edge. Yet, an interesting feature which appears downstream  $x/H = 0.3$  is the recovery, and even diminution, of  $\overline{v'v'}$  along the shear layer. A sudden enhancement due to the pulsed jet formation and convection at the initial stage is followed by a relaxation of velocity fluctuations.

It is worth to mention here that the difference of base pressure recovery between these forced wakes is not dramatic. The respective values of  $\gamma_p$  are 0.85 and 0.82 at  $Re_H = 3 \times 10^5$  representing a variation of only 3% on the base pressure. Hence, the modifications of these quantities are not as significant as their changes when compared to the natural flow. Meanwhile, we markedly note a lower vectoring effect and a smaller decrease of peak vorticity for the lowest jet amplitude, suggesting the importance of these parameters on the base pressure variation.

Part of the  $\langle \Gamma \rangle_\Omega$  circulation previously analyzed comes from the pulsed jet circulation  $\Gamma_j$ . The circulation flux issued from the exit slit may vary as  $(\Gamma_j)_{\text{flux}} \propto (V_{j\text{eff.}})^2$ , indicating indeed that higher jet velocities are capable to induces more deviated flow. However, the existence of an optimum jet amplitude on the  $\gamma_p$  evolution contradicts this tendency. The studies of Oxlade *et al.* (2015) show that this optimality is correlated to a further decrease of vorticity carried by the coherent jet structures discussed in figure 21. It is natural to conjecture that the complex generation of local swirling motions by the pulsed jets might have an additional influence in this process and should be addressed in future studies.

### 6.3. Upstream velocity effects: a global view of the forced wake

In this section, we analyze how the effects of actuation are modified by varying the upstream flow velocity  $U_o = 10, 15, 20 \text{ ms}^{-1}$  at fixed actuation parameters. For that, the pulsed jet amplitude is set to  $V_{j\text{eff.}} \sim 5.6 \text{ ms}^{-1}$ . This configuration corresponds to a 11% drag reduction when  $U_o = 15 \text{ ms}^{-1}$  or  $Re_H = 3 \times 10^5$ .

As illustrated in figure 24(a), the distribution of  $|\bar{v}|$  and the streamlines are highly influenced by the upstream velocity. A comparison between the unforced (full lines) and

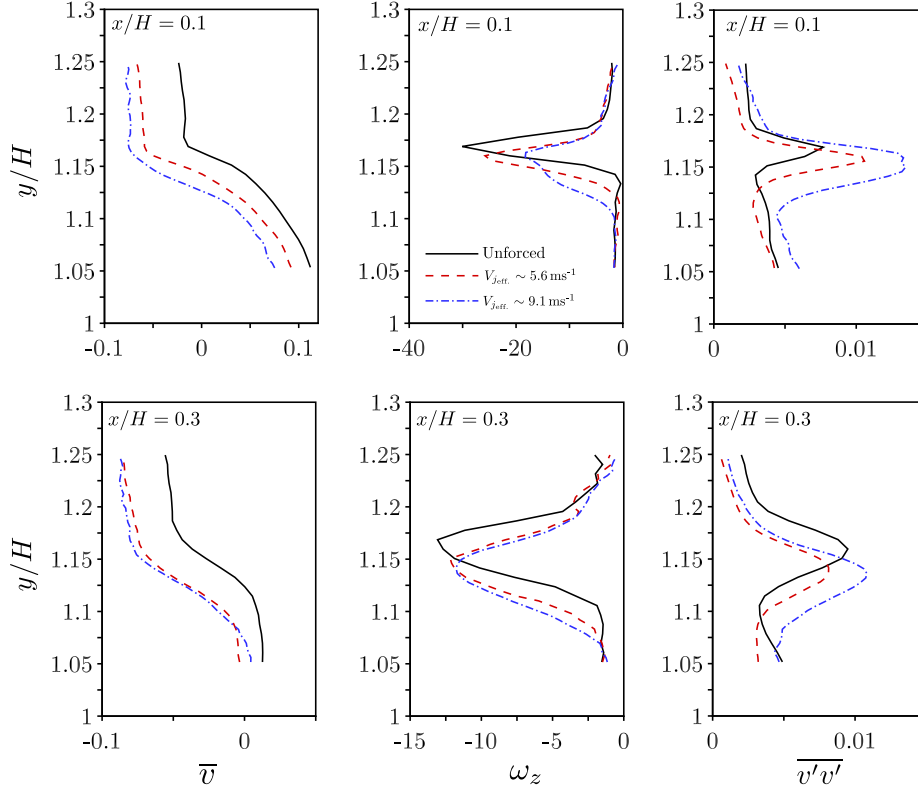


FIGURE 23. Influence of effective jet velocity for  $St_H = 12.1$  and  $Re_H = 3 \times 10^5$ . First row: (from left to right): profiles at  $x/H = 0.1$  of the time-averaged cross-stream velocity  $\bar{v}$ , time-averaged vorticity  $\omega_z$  and cross-stream velocity fluctuations  $\overline{v'v'}$  when  $V_{j,eff.} \sim 5.6, 9.1 \text{ ms}^{-1}$ . Similar effects for a further downstream streamwise position at  $x/H = 0.3$  are showed in the second row of the figure.

the forced (dashed lines) streamlines originated at  $(x/H, y/H) = (0, 1.17)$  shows that the flow deviation is stronger as we decrease  $U_o$ . We confirm this from the streamline velocity angle shown in figure 24(b). The streamwise evolution of  $\beta$  points out a change of the velocity field curvature due to an initial drop followed by a raise of the angle, which might associate a higher base pressure increase at lower upstream velocities. In figure 24(c), the increased downward velocity at the initial part of the shear layer is attested by velocity profiles ( $x/H = 0.02$ ). From the data in the region  $y/H > 1.17$ , we note that the entire boundary layer flow is deviated. The values of  $\bar{v}$  are doubled or triplicated when  $U_o$  decreases respectively from  $20 \text{ ms}^{-1}$  to  $15 \text{ ms}^{-1}$  or  $10 \text{ ms}^{-1}$ . The increase of flow deviation at low free-stream velocities has been also remarked in the experiments of Smith & Glezer (2002), where a main jet flow was deviated from the adjacent synthetic jets. From their time-response analysis, the increase of the synthetic jet velocity raises the vectored angle, in agreement to our previous data.

The actuation importantly affects the spread of vorticity and its growth along the shear-layer. Figure 25(a) shows the streamwise evolution of the peak vorticity  $(\omega_z)_{min}$ . The vorticity of the unforced flow decays as  $\omega_z \propto x^{-0.72}$ , in agreement with the turbulent separated boundary layer results from Morris & Foss (2003) showing an exponent of -0.79. The difference might be attributed to the absence of recirculating flow immediately

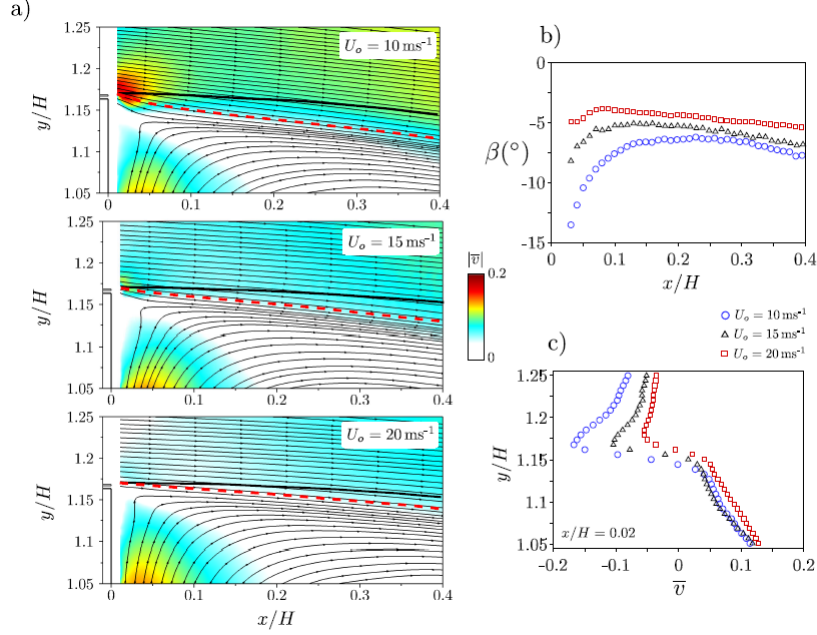


FIGURE 24. Effects of upstream Reynolds number on shear layer deviation: forced wake at  $St_H = 12.1$  and  $V_{j,eff} \sim 5.6 \text{ ms}^{-1}$ . a) Cross-stream velocity distribution  $|\bar{v}|$  and streamlines for varying  $U_o = 10, 15, 20 \text{ ms}^{-1}$  (from top to bottom). b) Streamwise evolution of the velocity angle  $\beta$  along the the separating streamlines indicated in a). c) Cross-stream velocity profile at  $x/H = 0.02$  presenting the higher velocity deviations at lower Reynolds number.

bellow the shear-layer because the authors studied a canonical separation from an edge. When control is applied, there is an overall decrease of the peak vorticity confirmed by the vorticity profile at  $x/H = 0.02$ :  $(\omega_z)_{\min}$  decreases by more than 30% at this streamwise location but further downstream ( $x/H > 0.25$ ) both evolutions collapse.

A diminution of  $(\omega_z)_{\min}$  along  $x$  is associated to an enlargement of the vorticity thickness  $\delta_{\omega_z}$ , defined as:

$$\delta_{\omega} = \frac{U_{\max} - U_{\min}}{\left| \frac{\partial \bar{u}}{\partial y} \right|_{\max}}. \quad (6.1)$$

For a canonical shear-layer flow,  $U_{\max} = U_o$ . In the present work, we must take into account the velocity of the recirculating flow which may impact, even slightly, the values of  $\Delta U = U_{\max} - U_{\min}$ . The streamwise evolution of  $\delta_{\omega_z}$  is plotted in figure 25(b). There is a decrease of the shear-layer growth ratio. Similar effects have been observed when the separated flow past a rounded ramp is actuated at high-frequency (Dandois *et al.* 2007), where the authors show a stabilizing effect of this forcing on the shear-layer dynamics. Finally, it is worth mentioning that this analysis has been carried out for  $U_o = 10, 20 \text{ ms}^{-1}$  with equivalent results (Barros 2015).

Given these changes of the vorticity growth ratio, we would expect different dynamics along the shear-layer. Let us analyze now its turbulent statistics. Figure 26(a) displays the distribution of the turbulent kinetic energy  $k = 0.5 \times (\overline{u'u'} + \overline{v'v'})$  - more precisely, the two contributions to  $k$  measured with the PIV system - for both flows when  $U_o = 15 \text{ ms}^{-1}$ . The unforced, natural evolution of the shear layer is associated to a raise of  $k$  along  $x$ . When forcing is applied, it induces an initial increase of turbulent kinetic energy up to



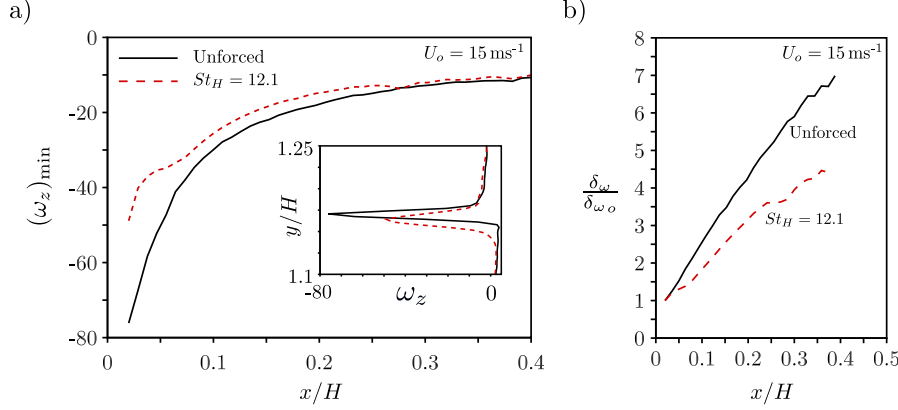


FIGURE 25. Spanwise vorticity decay along the streamwise direction. a) Decay of the peak vorticity  $(\omega_z)_{\min}$  along  $x$  and vorticity profile at  $x/H = 0.02$  close to the model edge for both unactuated and forced flows. The forcing parameters are  $St_H = 12.1$  and  $V_{j\text{eff.}} \sim 5.6 \text{ ms}^{-1}$  when  $U_o = 15 \text{ ms}^{-1}$ . b) Streamwise growth of the vorticity thickness  $\delta_{\omega_z}$  and  $\delta_{\omega_o}$  is the initial value.

$x/H \sim 0.13$ , downstream which a damping of  $k$  is noticed. The initial growth of  $\overline{v'v'}$  is particularly confirmed in the vicinity of the edge due to the pulsed jet emission (see inserted figure).

As reported in figure 26(b), the initial increase of  $k_{\max}$  promoted by actuation is damped up to a critical position where both configurations present equivalent values. This location varies with the upstream velocity, its values being  $x = 0.07, 0.13, 0.25$  respectively for  $U_o = 10, 15, 20 \text{ ms}^{-1}$ . It could be explained by a higher convective velocity of the formed jets with the increase of  $U_o$ . Further downstream,  $k_{\max}$  is smaller than the unforced flow, indicating an stabilization of the cross-stream dynamics. By analyzing the peak values of the Reynolds shear stresses  $\overline{u'v'}_{\min}$ , this behavior is preserved as we see in the plot of figure 26(c), where a reduction of  $|\overline{u'v'}_{\min}|$  is observed under forced conditions. An additional feature is a sudden augmentation of  $\overline{u'v'}_{\min}$  at  $x/H \sim 0.03$  followed by a drop up to the fluctuations damping.

Dandois *et al.* (2007) and Vukasinovic *et al.* (2010) have remarked the same stabilizing behavior of shear-layers submitted to high-frequency forcing. An initial increase of fluctuations due to the flow pulsation was followed by a downstream damping of flow activity. By analyzing the time-averaged streamwise velocity profiles, Dandois *et al.* (2007) performed linear stability analysis to conclude that the main effect of the high-frequency forcing is a decreasing of the growth rates obtained from the most amplified shear-layer modes. On the other hand, Vukasinovic *et al.* (2010) showed the presence of high-dissipation zones at the vicinity of actuation and claimed that this zone somehow drains energy from the mean flow leading to a stabilization, in what they call a dissipative small scale actuation.

Motivated by their studies, we compute a contribution to the time-averaged turbulent kinetic energy production  $\Pi(x, y)$  using the two components of the velocity field obtained by PIV:

$$\Pi = -\overline{u'u'} \left( \frac{\partial \bar{u}}{\partial x} \right) - \overline{v'v'} \left( \frac{\partial \bar{v}}{\partial y} \right) - \overline{u'v'} \left( \frac{\partial \bar{u}}{\partial y} + \frac{\partial \bar{v}}{\partial x} \right). \quad (6.2)$$

Profiles of  $\Pi$  for the presently studied Reynolds numbers are illustrated in figure 27. The selected streamwise positions correspond respectively to the beginning of the shear-



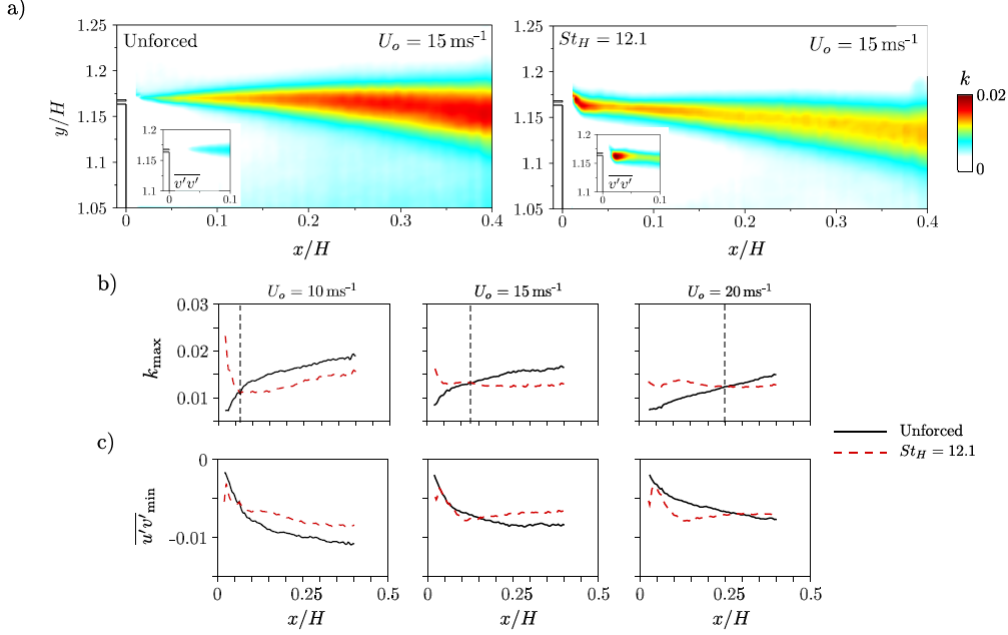


FIGURE 26. Turbulent kinetic energy  $k$  and Reynolds stresses along the upper shear layer in the vicinity of the edge. a) Contour maps of  $k$ . The inserted picture indicates the cross-stream velocity fluctuations  $\overline{v'v'}$  near the exit slit. b) Streamwise evolution of  $k_{\max}$ . The vertical dashed lines are located at  $x = 0.07, 0.13, 0.25$  corresponding to the positions where both unforced and actuated flow present the same  $k_{\max}$ . c) Streamwise evolution of the minimum shear Reynolds stress  $\overline{u'v'}_{\min}$ . The forcing conditions are  $St_H = 12.1$  and  $V_{j\text{eff}} \sim 5.6 \text{ ms}^{-1}$ , with the upstream flow velocity equals to  $U_o = 15 \text{ ms}^{-1}$ .

layer, where the actuation significantly increase  $k$ ; the position in which  $k_{\max}$  is approximately the same for both unactuated and actuated flows; and finally a location where the damping of the velocity fluctuations is established close to the end of the PIV domain.

At the initial location, whatever the value of  $U_o$ , the production term of the actuated flow is more than twice the peak values of the reference case. Then a reduction of  $\Pi$  appears at intermediate streamwise positions. Finally, further downstream, the maximum of the production profiles decreases by up to 30% for  $U_o = 10, 15 \text{ ms}^{-1}$  and about 15% when  $U_o = 20 \text{ ms}^{-1}$ . These results are in close agreement to the decrease of energy production discussed in Dandois *et al.* (2007) and Vukasinovic *et al.* (2010), indicating that the mechanisms of the high-frequency actuation are quite general.

Up to now, we have studied the effects of the high-frequency forcing on the shear-layer close to the upper edge. A global change of the whole wake dynamics might be expected due to the variations of the shear growth. Within this context, we extend our analysis to the entire near wake flow by means of the largest PIV field of view. We report in figure 28(a) the cross-stream velocity fluctuations  $v'v'$  and the turbulent kinetic energy integrated across the wake:

$$K(x) = \int_{y_{\min}}^{y_{\max}} k(x, y) dy. \quad (6.3)$$

These quantities are calculated for two regions around the top and the bottom shear-layers. Not only the reduction of  $K$  is observed along the upper part, as reported before

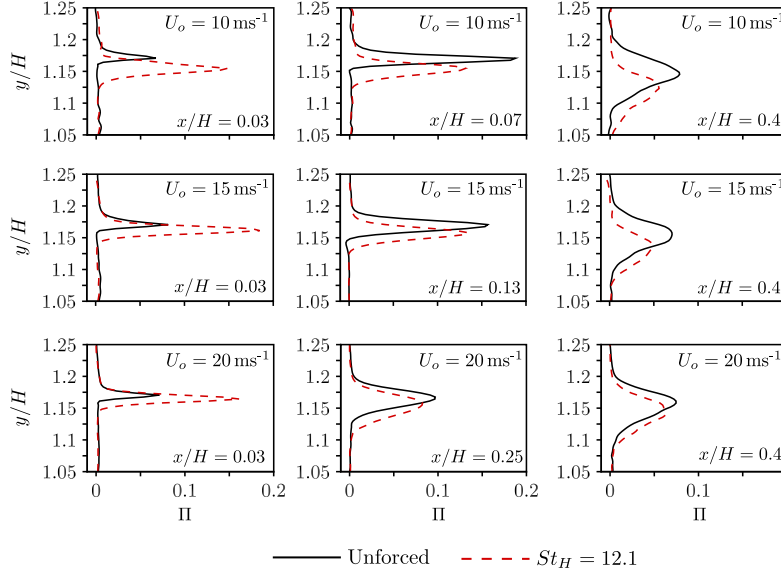


FIGURE 27. Cross-stream profiles of turbulent kinetic energy production  $\Pi$  at several stream-wise locations and for varying Reynolds numbers. The forcing parameters are  $St_H = 12.1$  and  $V_{j\text{eff.}} \sim 5.6 \text{ ms}^{-1}$ .

using time-resolved PIV, but also along the bottom development of the wake. Similar trends are obtained when  $U_o = 10$  or  $20 \text{ ms}^{-1}$ . A more pronounced decrease of velocity fluctuations is confirmed for the lowest upstream velocity.

Based on the results presented in § 5, the changes in cross-stream fluctuations is related to the entrained flow inside the wake. We evaluate its physical measure by displaying  $\mathcal{V}_+$  and  $\mathcal{E}$  in figure 28(b) at a Reynolds number  $Re_H = 3 \times 10^5$ .

When actuation is applied, a decrease of the cross-stream motions and the total kinetic energy of the reverse flow is observed. These effects are also confirmed by measurements when  $Re_H = 2$  or  $4 \times 10^5$  (not shown here for brevity). Interestingly, there is a decrease of  $\mathcal{V}_+$  very close to the model's rear surface, highlighting a diminution of upward flow adjacent to the rear surface of the model and suggesting a decrease of the entire recirculating flow intensity inside the wake. Correspondingly, the total kinetic energy of the reverse flow presents a diminution along the entire bubble.

It is important to remark that the analyzed quantities are computed in the symmetry plane of the wake and gives only an order of the real measure of the entrained flow, which in reality is three-dimensional. From the presented results, however, there is a strong evidence that these quantities provides us crucial information about the wake entrainment.

We turn our attention now to the modifications of wake topology. The stream traces of the natural and forced wakes at  $Re_H = 3 \times 10^5$  are depicted in figure 29(a). The limit of the bubbles corresponds to the recirculation length  $L_r$ . Albeit a 15 % increase of base pressure, only a very slight increase of the mean recirculation bubble in the symmetry plane is computed for actuation at  $St_H = 12.1$   $V_{j\text{eff.}} \sim 5.6 \text{ ms}^{-1}$  at this Reynolds number. The recirculating bubble is increased by at most 2–4 % considering all upstream velocities. To compare with the low-frequency actuation, the studied forcing at  $St_H \sim 0.8$  - leading to a decrease of 12 % on  $\langle \overline{C_p} \rangle$  - decreases the bubble by more than 10 %.

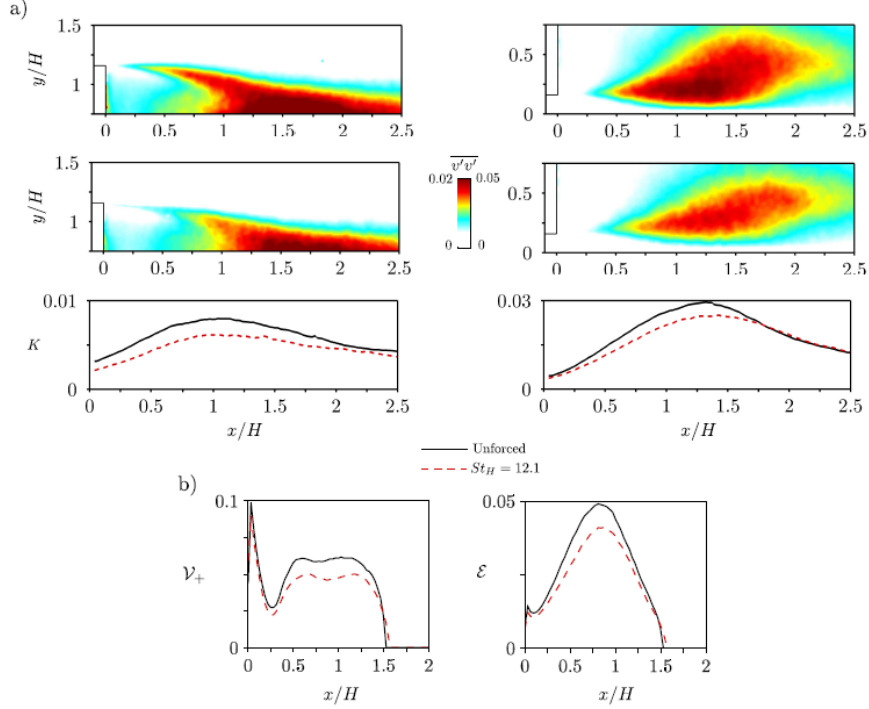


FIGURE 28. Velocity fluctuations on the near wake from the extended PIV field of view and entrainment measure. a) Contour maps of  $\overline{v'v'}$  for both the upper and the bottom shear-layers. Streamwise evolution of  $K$  (defined in the text). b) Streamwise evolution of  $V_+$  and  $\mathcal{E}$  inside the region of reverse flow up to the end of the recirculating region limited by  $x = L_r \sim 1.5$ . The forcing conditions are  $St_H = 12.1$  and  $V_{j,eff.} \sim 5.6 \text{ ms}^{-1}$ . The upstream Reynolds number is  $Re_H = 3 \times 10^5$ .

Surprisingly, at least by regarding the streamlines, we do not observe significant changes on the wake topology despite a decrease of drag of 11%.

A careful analysis of the streamwise velocity  $\bar{u}$  contours, however, sheds light on the fine modifications of the wake geometry. In figure 29(b), the contour lines corresponding to iso-values of streamwise velocity  $\bar{u} = \{-0.25, 0.25, 0.65\}$  are shown respectively for  $U_o = \{10, 15, 20\} \text{ ms}^{-1}$ . We observe a narrowing of the wake, which is more pronounced when  $U_o = 10 \text{ ms}^{-1}$ , in agreement with the highest flow deviations measured at the vicinity of model's edge at this upstream velocity. It is also noticeable the deviation of the flow along the bottom shear layer, which confirms that it is equally vectored due to the actuation along all edges. Similar conclusions have been measured with respect to the lateral shear-layers (Barros *et al.* 2014).

To characterize the streamwise development of the bottom part of the wake, a measure of the maximum streamwise velocity originated from the underflow is presented in figure 29(c), where a smaller decay of  $\bar{u}_{max}$  is attested for the actuated flows, in agreement to the lower values of  $\overline{v'v'}$  in this region. Besides, the decay is modified by the upstream velocity  $U_o$ , where smaller momentum losses are measured for  $U_o = 10 \text{ ms}^{-1}$ . For the sake of completeness, we plot the velocity profiles indicating the total momentum deficit at the end of the PIV domain  $x/H = 2.48$  for all configurations in figure 29(d), and we verify the recovery of momentum along the wake when high-frequency forcing is applied.

Finally, we study the effects of the forcing on the global wake mode measured down-

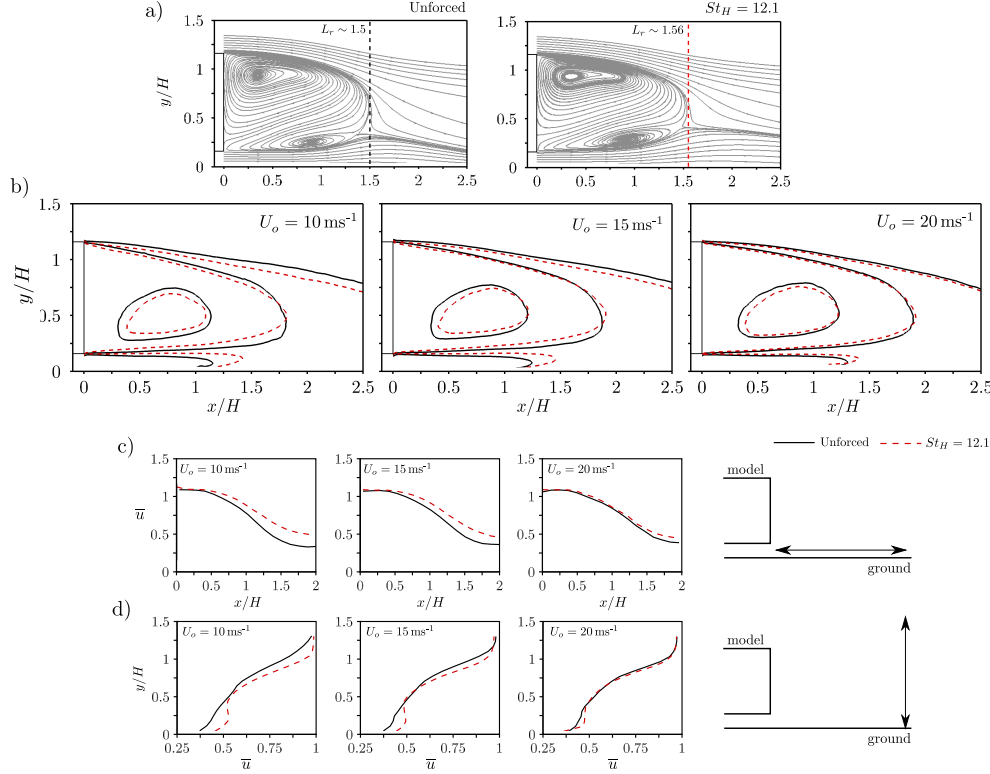


FIGURE 29. Global wake topology and effects of high-frequency actuation. a) Stream traces of the in plane velocity field ( $U_o = 15 \text{ ms}^{-1}$ ). b) Streamwise velocity contours  $\bar{u} = \{-0.25, 0.25, 0.65\}$  indicating a narrowing of the wake. c) Decay of the maximum time-averaged streamwise velocity  $\bar{u}_{\max}$  along  $x$ . d) Streamwise velocity profiles at the end of the PIV field of view  $x/H \sim 2.5$  showing the velocity and momentum deficit. The actuation conditions are  $St_H = 12.1$  and  $V_{j\text{eff.}} \sim 5.6 \text{ ms}^{-1}$ .

stream the end of the recirculating bubble. From point wise measurements at  $x/H = 2$  and  $x/H = 3$ , figure 30 presents the power spectral densities of the streamwise velocity measured by a single hot-wire probe in the symmetry plane ( $y/H = 0.9$ ) and at a horizontal plane ( $y/H = 0.6$  and  $z/H = 0.5$ ) parallel to the ground. No significant modifications are observed on the shedding frequencies, differently to what is discussed at lower-actuation frequencies by the authors (Barros *et al.* 2015). However, a close inspection reveals a slight decrease of the power peak when control is applied, indicating these modes are modestly damped due to the effects of forcing up to the end of the recirculating flow, where these oscillations becomes easily identified for this geometry Grandemange *et al.* (2013).

#### 6.4. A conceptual scenario for high-frequency actuation

The phenomenology of the high-frequency pulsed jets previously discussed puts in evidence the flux of circulation in the vicinity of the model's edge responsible to deviate the shear-layer. In the following, we propose a conceptual scenario which attempts to clarify the dependence of this flow deviation on the jet parameters and upstream conditions.

Figure 31 illustrates the trailing-edge and its adjacent region filled with clockwise circulation during the high-frequency forcing. We assume the flow deviation depends on the enhanced entrainment up to a distance  $l_\Omega$  from the model's edge. The region  $\Omega$  must

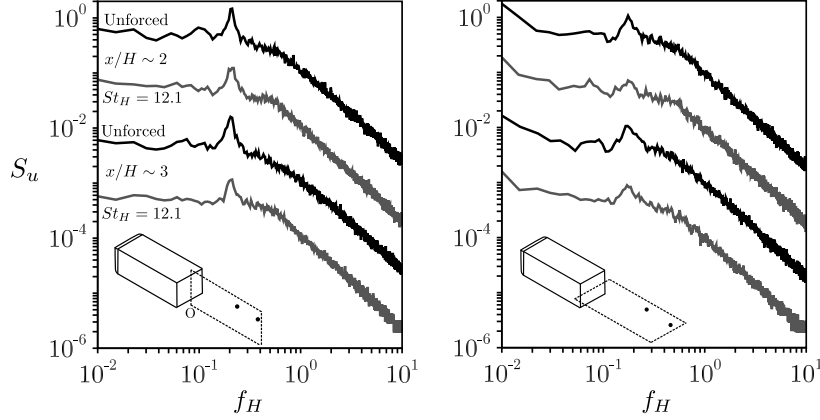


FIGURE 30. Oscillatory dynamics downstream the recirculating region at  $Re_H = 3 \times 10^5$ . a) Global modes in the symmetry plane issuing from the interaction of the top and bottom shear layers. The dots represent the specific measurement locations  $x/H = 2$  and  $x/H = 3$  at  $y/H = 0.9$ . b) Global modes in a horizontal plane from the interaction of the lateral shear layers. The dots represent the locations  $x/H = 2$  and  $x/H = 3$  at  $y/H = 0.6$  and  $z/H = 0.5$ . The forcing parameters are  $St_H = 12.1$  and  $V_{j\text{eff.}} \sim 5.6 \text{ ms}^{-1}$ .

be viewed as a sensitive zone susceptible to flow deviation by the generated circulatory motions. On the contrary, for distances greater than  $l_\Omega$ , the convection of the pulsed jets lead to entrainment in the bubble region decreasing the model's base pressure (low-frequency forcing).

The circulation  $\Gamma_\Omega$  produced in this domain induces the cross-stream velocity  $v_{\text{ind.}}$  causing the flow deviation  $\beta_{\text{ind.}} = (v_{\text{ind.}}/U_\delta)$ , in which  $U_\delta$  is the boundary layer velocity close to the edge and proportional to  $U_o$ . By considering an analogy to the velocity induced by a potential vortex, we assume  $\beta_{\text{ind.}} \propto \Gamma_\Omega/(U_o d)$ , where  $d$  is related to the slit centerline position with respect to the outer surface adjacent to the boundary layer.

In particular, the amount of  $\Gamma_\Omega$  crucially depends on the circulation from each pulsed vortex  $\Gamma_j$  and its convection outside the domain. Following Dabiri (2009), we may write  $\Gamma_j = 0.5 T_f V_{j\text{eff.}}^2$ , where  $T_f$  is the formation time after which the circulation does not enter the main vortex head. The pulsed jet circulation will be convected with a certain velocity  $U_c \sim \mathcal{F}(U_\delta, U_r, V_j)$  dependent on the boundary layer as well as the recirculating flow, both increasing with  $U_o$ . During a period of actuation  $T_i$ , the convected distance is loosely  $l = U_c T_i$ : when  $l$  becomes too large when compared to  $l_\Omega$ ,  $\Gamma_\Omega$  decreases in average leading to a reduction of  $\beta_{\text{ind.}}$ . This happens when the upstream flow is faster (increase of  $U_o$ ) or when the period of actuation is high (lower actuation frequency).

By coupling both the circulation production and its convection, the dependence of  $\beta_{\text{ind.}}$  can be stated:

$$\beta_{\text{ind.}} \sim \mathcal{F} \left[ \left( \frac{T_f V_{j\text{eff.}}^2}{U_o d} \right), \left( \frac{l_\Omega}{U_c T_i} \right) \right]. \quad (6.4)$$

Some conclusions drawn from the presented results might be supported by this relation. First, keeping all quantities fixed, the increase of jet velocities up to the critical  $V_{j\text{eff.}}$  leads to an augmentation of the main vortex head circulation  $\Gamma_j$ . From our relation, this is intimately linked to an increase of  $\beta_{\text{ind.}}$  and an intensification of the fluidic boat-tailing effect leading to a pressure recovery. On the other hand, by increasing  $U_o$  for fixed jet parameters, the flow convects more rapidly the pulsed jets outside the domain

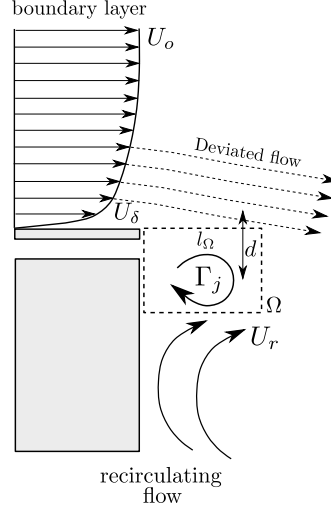


FIGURE 31. Conceptual sketch of the high-frequency actuation and its effect on the shear-layer deviation. See text for details.

$\Omega$ , leading to a reduction of the total circulation in this region consequently decreasing  $\beta_{\text{ind.}}$ . This is confirmed from the smaller vectoring angles  $\beta$  measured at higher upstream flow velocities.

We have not explicitly indicated the influence of the slit thickness  $h$ , but it implicitly impacts  $T_f$ . From the piston-cylinder vortex rings literature,  $T_f$  would vary as  $T_f \sim hT^*/V_j$ , where  $T^*$  is universal for each pulsating geometry (Gharib *et al.* 1998; Dabiri 2009). Then, we observe an additional effect of increasing  $V_j$ : it occasionally may provoke vortex pinch-off and stop the transfer of circulation from the jet boundary layers to the main vortex head. In this sense we could imagine the optimality of  $V_{j_{\text{eff.}}}$  somehow linked to vortex pinch-off given the formation time-scales as discussed in Gharib *et al.* (1998). This complex process, however, may limit our dimensional and physical analysis implying a more complex model to predict the flow vectoring effect. Further measurements with systematic varying parameters should be performed for a complete scenario. The study of Oxlade *et al.* (2015) gives some hints correlating the vorticity (circulation) of the main vortex head and its saturation for a critical value of  $V_j$ , in agreement with our hypothesis.

In order to make a parallel to the low-frequency actuation effects on the drag, the high-frequency forcing impacts the wake by two main process. First, there is an initial flow deviation close to the edges and a narrowing of the whole wake. Second, the generation of a vortex train somehow stabilizes the shear-layer growth leading to an overall reduction of the turbulent kinetic energy and a decrease of entrained flow. From the initial vectoring, we would expect not only a narrowing of the wake but also a diminution of the recirculating length. However, what we observe is indeed a very similar wake length when compared to the reference flow. This can be explained by the fact that the reduced velocity fluctuations acts to elongate the bubble length by reducing the entrained flow. The resulting wake bubble presents then a higher aspect ratio  $L_r/H^*$  by the diminution of  $H^*$ , differently to the low actuation frequency where an enhancement of the entrainment process decreases  $L_r$ . Both scenarios appears to be in agreement with the ideas of Gerrard (1966) and Roshko (1993a), where conceptual models for wake entrainment and base pressure are respectively proposed.

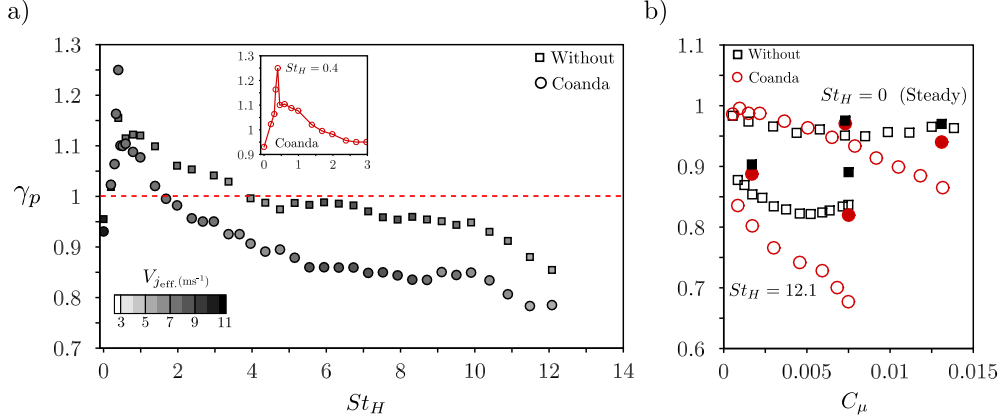


FIGURE 32. Impact of unsteady Coanda blowing on the base pressure. a) Comparison between the use or not of the Coanda surface on the base pressure parameter  $\gamma_p$  by varying the actuation frequency  $St_H$  at  $Re_H = 3.0 \times 10^5$ . The measurements are taken with a fixed input pressure  $P_i$  of 1.45 bar. b) Effects of the momentum coefficient  $C_\mu$  for the steady ( $St_H = 0$ ) and high-frequency forcing ( $St_H = 12.1$ ) on  $\gamma_p$  (open symbols) and  $\gamma_d$  (filled symbols) selected for some configurations.

## 7. Unsteady Coanda blowing and its effect on the drag

We are now able to apply the concepts of periodic actuation by coupling the unsteady pulsed jets with the so-called Coanda effect (Wille & Fernholz 1965). As discussed in § 2, a quarter of disk with radius  $r = 9h$  is installed immediately below the jet slit. The choice of this geometry is based on previous experiments where the Coanda effect was implemented for drag reduction in axisymmetric geometries (Freund & Mungal 1994; Abramson *et al.* 2011) and square-back vehicles (Englar 2001; Pfeiffer & King 2012). Our aim here is to characterize the role of the unsteady Coanda forcing within the context of bluff body drag reduction.

### 7.1. The impact on the base pressure and wake flow

In figure 32(a), the global effects of unsteady Coanda blowing are presented by the  $\gamma_p$  changes with  $St_H$  when the Reynolds number is  $Re_H = 3.0 \times 10^5$ . The Coanda blowing obeys a similar trend when compared to the pulsed jets without the curved surface (added for comparison). The discrete peak revealing the sudden decrease of base pressure at  $St_H \sim 0.4$  is preserved for this configuration and detailed in the inserted picture. At this forcing frequency, the base pressure drops by 25 %. The range of frequencies decreasing the base pressure remains relatively comparable to the no-Coanda situation. It is however reduced to the interval  $St_H \in [0.1, 1.5]$ . Overall, the maximum decrease of base pressure at low-frequencies is about 10 %. Interestingly, the base pressure recovery starts earlier from  $St_H \sim 2.0$  and extends to  $St_H \sim 12$ : for the tested jet amplitudes, the Coanda forcing outperforms with a nearly constant gain leading to a shifted curve towards lower values of  $\gamma_p$ .

To quantify the influence of the jet amplitude on  $\gamma_p$ , we select the steady ( $St_H = 0$ ) and the high-frequency ( $St_H = 12.1$ ) blowing configurations and vary the momentum coefficient  $C_\mu$ . The data is reported in figure 32(b) where we select some configurations to measure the drag force and compute  $\gamma_d$  (see filled symbols and the figure caption). Without the presence of the curved surface, steady blowing increases the base pressure by approximately 5 %, reducing the model's drag by at most 3 % in the range  $C_\mu \in [0, 0.015]$ ,

leading to blowing velocities  $\bar{V}_j/U_o \in [0, 1.1]$ . This performance agrees with past results applying similar steady jet amplitudes in axisymmetric or square-back models (Freund & Mungal 1994; Wassen *et al.* 2010; Krentel *et al.* 2010). While no difference is measured up to  $C_\mu \sim 7.5 \times 10^{-3}$  ( $\bar{V}_j/U_o \sim 0.55$ ), steady Coanda blowing improves the base pressure recovery at higher blowing velocities. For example, when  $C_\mu = 13.1 \times 10^{-3}$  corresponding to  $\bar{V}_j/U_o \sim 1.0$ , base pressure increases by 14 % ( $\gamma_p = 0.86$ ) and drag decreases by 6 % ( $\gamma_d = 0.94$ ) showing comparable results to the works from Pfeiffer & King (2012). The curve indicates that further increase of base pressure might be achieved using higher blowing velocities, similarly to the trends shown by Englar (2001) and Pfeiffer & King (2012).

We equally obtained an improved performance using high-frequency Coanda blowing, reaching the optimal  $\gamma_p = 0.67$ , corresponding to 33% of base pressure increase when  $C_\mu = 7.5 \times 10^{-3}$  with a total drag reduction of 18 %. Curiously, there is no saturation of the high-frequency Coanda actuation, indicating a monotonic tendency as observed for the steady control. One may hypothesize that the shear-layer vectoring is mainly dictated by the new boundary conditions imposed by the curved geometry, modifying the relation to the pulsed jet circulation discussed in the previous section.

In order to attest the flow deviation imposed by the Coanda effect, we display the contour-maps of time-averaged cross-stream velocity  $\bar{v}$  in figure 33. The unforced flow together with the steady blowing at  $C_\mu = 13 \times 10^{-3}$  ( $\gamma_p \sim 0.85$ ) and the high-frequency Coanda blowing at  $C_\mu = 7.5 \times 10^{-3}$  ( $\gamma_p \sim 0.67$ ) are selected for analysis. The superiority of the unsteady forcing in deviating more flow when compared to the steady jets appears evident from the distribution of  $|\bar{v}|$ : it is indeed verified by analyzing the vorticity contours illustrated in detail. Besides, we note a reduction of the upward velocity surrounding the rear surface, confirming the same behavior of the previously analyzed high-frequency configuration.

When comparing the steady blowing to the periodic Coanda actuation, attention must be paid to the importance of the jet unsteadiness on flow attachment along the rounded surface. Although the unsteady forcing with frequency  $St_H = 12.1$  presents a smaller averaged  $C_\mu = 7.5 \times 10^{-3}$ , the instantaneous jet velocity may reach about 3 times its mean value, as exemplified in figure 4(a). Hence, the time evolution of the momentum flux competing with the pressure gradient imposed by the rounded surface plays a significant role on the flow mechanisms leading to the unsteady Coanda attachment (Jukes & Choi 2009). The use of steady blowing at velocities similar to the maximum jet amplitudes during the unsteady cycle would therefore be necessary to compare the effects of both actuation on flow attachment. Yet, this was not possible in the present study due to the needed input pressure  $P_i$ , beyond the limits of the pulsed jet system apparatus. Moreover, generating a steady jet for such control would require a large amount of power, considerably affecting the energy balance. This aspect is commented in what follows.

Let us describe the time response of the high-frequency Coanda blowing by performing a transient analysis from the unforced flow to the controlled wake. The time evolution of the top pressure coefficient  $C_{p_T}$  is depicted in figure 34(a) as well as the corresponding velocity vectors colored by the streamwise velocity  $u$ . The total time window displayed is 0.1 s, which corresponds to 5 convective time units ( $t^* = tU_o/H$ ) or 1 shedding cycle from  $f_{n_o} \sim 0.2$ . The initial raise of  $C_{p_T}$  takes approximately 6 actuation cycles ( $\sim 0.01$  s) to be established, after which a decrease of pressure is noted due to the rapid stabilization of  $P_i$  in the compressed air reservoir †. This time interval is equivalent to 0.5 wake convective

† All the time-averaged measurements presented along the present work are performed at least 5 s following this stabilization, whose duration is roughly 0.05 s.



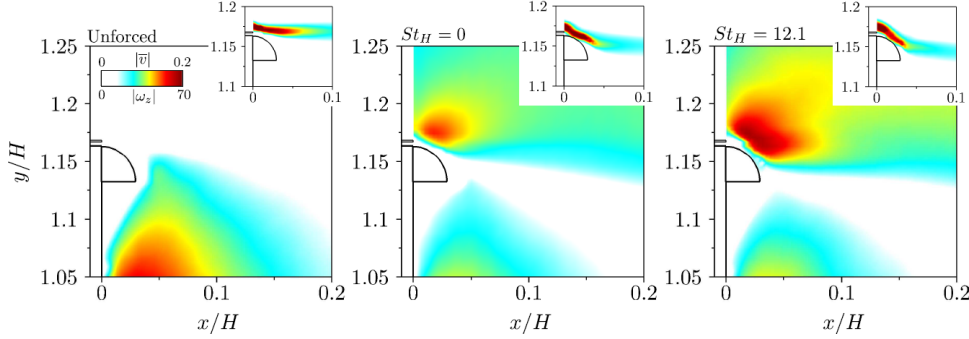


FIGURE 33. Time-averaged cross-stream velocity  $|\bar{v}|$  and vorticity  $|\omega_z|$  fields. Comparison between the unforced flow (left), the steady forcing  $St_H = 0$  ( $C_\mu = 13 \times 10^{-3}$ ) and the high-frequency Coanda blowing  $St_H = 12.1$  ( $C_\mu = 7.5 \times 10^{-3}$ ).

units, indicating the increase of pressure scales with the rapid wake adjustment by the shear-layer Coanda attachment.

The snapshots emphasize the correlation between the increase of base pressure and an abrupt change of the velocity field curvature, as indicated in the right picture where the flow starts to deviate very close to the Coanda surface. It strongly suggests that one important effect responsible for the base pressure recovery is linked to the wake topology and curvature variations. We consider now the transition of the spatially integrated base pressure  $\langle C_p \rangle$  in figure 34(b) when the control is turned-off. Although PIV fields are not obtained during this transient, we observe a slow recovery during approximately 5 convective time units (0.1 s) up to the unforced pressure value, suggesting a period of reestablishment of the initial wake conditions by the detachment of the flow from the Coanda surface.

As shown in precedent discussions, high-frequency actuation modifies the initial growth rate of the shear-layers resulting in the stabilizing effect of velocity fluctuations along the entire wake. Given the very similar trends pointed out from the unsteady Coanda effects on the base pressure, we may question if the global wake properties still present similar features. In figure 35(a), the integrated turbulent kinetic energy ( $K$ ) is reported showing an overall decrease of velocity fluctuations along the streamwise wake. As an example,  $K$  decreases by more than 20 % at  $x/H \in [0.8, 1.5]$ . The total kinetic energy  $\mathcal{E}$  inside the reverse flow also presents a similar behavior, as shown in figure 35(b), with reductions of up to 30 %. Finally, we integrate the reverse streamwise velocity as:

$$\mathcal{M} = \int_{\Omega_{\{\bar{u} < 0\}}} |\bar{u}| dy, \quad (7.1)$$

and plot  $\mathcal{M}$  in figure 35(c). Part of the calculated decrease of  $\mathcal{E}$  comes from the streamwise reverse flow intensity, which is equally reduced for this flow. It indicates an order of the reverse mass flow inside the wake, in agreement to the decrease of entrained fluid inside the wake.

In summary, the unsteady Coanda blowing contributes to the base pressure not only by amplifying the shear-layer deviation but also by preserving the stabilizing effect of the shear-layers from high-frequency forcing, which results in a less-fluctuating wake with lower entrainment.

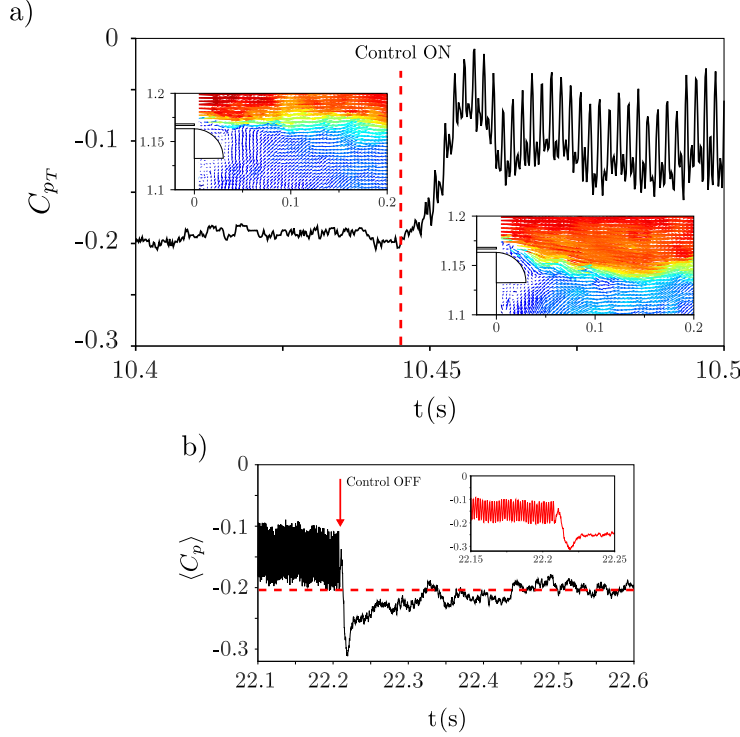


FIGURE 34. Transient analysis at high-frequency Coanda forcing. a) Time-response of the top pressure sensor when control is performed at  $St_H = 12.1$  ( $C_\mu = 7.5 \times 10^{-3}$ ) for an upstream velocity  $U_o = 15 \text{ ms}^{-1}$ . b) Transient analysis when control is turned-off revealing the time-scales of the integrated base pressure  $\langle C_p \rangle$  response. The horizontal dashed line represent the unforced pressure coefficient from longer time-averaged measurements.

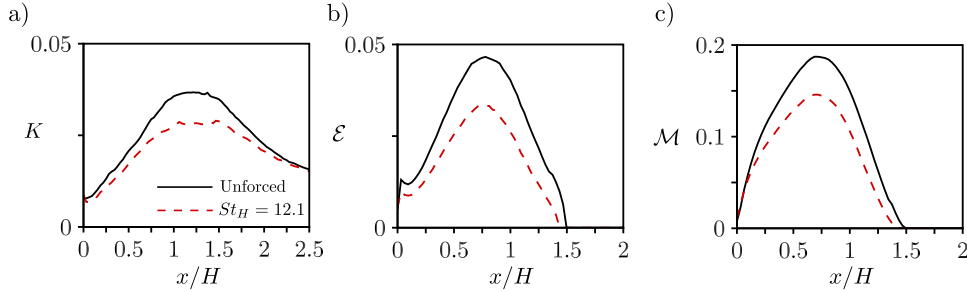


FIGURE 35. Global measurements in the near wake. Integrated turbulent kinetic energy  $K$  (a), total kinetic energy inside the reverse flow region  $\mathcal{E}$  (b) and integrated reverse streamwise velocity  $\mathcal{M}$  (c). The actuation parameters are  $St_H = 12.1$  and  $C_\mu = 7.5 \times 10^{-3}$  with the Coanda effect.

### 7.2. An evaluation of the flow control energy input

One would ask the necessary energy from the pulsed jets capable to recover the base pressure and modify drag. More importantly, a relation of this power to the recovered energy from drag reduction must be established for flow control purposes. To this end, a selection of forced wakes is done to evaluate the pulsed jet energy and drag variations. Following the power analysis discussed in past studies (Freund & Mungal 1994; Choi *et al.* 2008; Pfeiffer & King 2012), we may define the power ratio  $\zeta$  as:

---

$St_H$ -Configuration	$V_{j\text{eff.}} (\text{ms}^{-1})$	$C_\mu (\times 10^{-3})$	$\gamma_p$	$\gamma_d$	$\overline{V_j^3} (\times 10^3, \text{m}^3\text{s}^{-3})$	$\zeta$
0- Steady	11.5	7.3	0.95	0.97	1.54	1.54
0- Steady	15.8	13.1	0.96	0.97	4.00	0.59
12.1- HF	5.6	1.7	0.85	0.9	0.23	34.5
12.1- HF	11.6	7.5	0.84	0.89	2.74	3.3
0- Steady, Coanda	11.5	7.3	0.95	0.98	1.54	1.02
0- Steady, Coanda	15.8	13.1	0.86	0.94	4.00	1.18
12.1- HF, Coanda	5.6	1.7	0.80	0.89	0.23	38
12.1- HF, Coanda	11.6	7.5	0.67	0.82	2.74	5.17

---

TABLE 4. Power ratio parameter for drag reduction with or without the Coanda effect.

$$\zeta = \frac{|1 - \gamma_d| C_{x_o} S U_o^3}{s_j \overline{V_j^3}}. \quad (7.2)$$

It is worth mentioning that the power necessary to maintain the compressed air  $P_i$  in the reservoir as well as the electrical energy spent to actuate the valves are not taken into account here. We are mainly concerned with the jet mechanical energy compared to the drag power. Table 4 reports the quantities used to compute  $\zeta$  for several drag reducing configurations using steady or high-frequency (HF) Coanda blowing.

Except the high momentum steady blowing, all calculated ratios  $\zeta$  are greater than the unity, showing a recovery of energy invested on actuation by drag reduction. Generally, as expected from the base pressure measurements, the highest efficiency corresponds to the HF forcing configurations in the presence or not of the Coanda surface. The best compromise between the power recovered and injected energy comes with the actuation at low momentum coefficient  $St_H = 12.1$  and  $C_\mu = 1.7 \times 10^{-3}$ : the values of  $\zeta$  are 34 and 38 respectively with the use or not of the Coanda effect. The high values of  $\zeta$  are linked to the low exit jet velocities in these configurations, which significantly impact  $\zeta$  due to the cubic dependence on  $V_j$ . The configuration with the higher drag reduction of 18%  $\gamma_d = 0.82$  is the high-frequency Coanda blowing, corresponding to an energy saved five times greater than the pulsed jet energy.

From these results, unsteady Coanda blowing appears to be a promising strategy for further development and optimization in view of future applications in bluff body drag reduction. Despite the fact that it was tested only for the present radius geometry, parametric variations of  $r$  at different upstream conditions  $U_o$  would bring more insights on the influence of the attachment point along the surface in order to improve drag reduction and power saving.

## 8. Concluding remarks

In the present study, we investigate the effects of periodic forcing on the wake and drag of a simplified blunt vehicle. For that, pulsed jets are blown at the trailing-edges of the model and tangentially to the main flow. By the measurements of drag, base pressure and velocity fields from particle image velocimetry, the effects of this control technique are analyzed revealing mainly two flow phenomena with distinct time-scales.

First, when actuation is applied within a range of frequencies close to the natural wake instabilities, drag increases by approximately 10 % due to an overall decrease of the base-line pressure. The convection of the pulsed jet structures amplify the shear-layer cross-stream dynamics by the generation of large-scale eddies. The resulted engulfing motions

lead to an enhancement of the flow entering the bubble region, principally shortening the wake length. As a result, the intense recirculating flow generates low-pressure zones on the rear surface of the body leading to a raise of its drag.

The increase of the forcing frequency shifts the mixing upstream towards the edges of the model. In this region, an accumulation of the circulatory motions issued from the periodic vortices induces a deviation of the initial separated shear-layer, creating what we refer to a *fluidic boat-tailing* effect, in an analogy to the homonym passive control device (Choi *et al.* 2014). A conceptual model is proposed to clarify how the free-stream conditions and the jet parameters impact the flow deviation: the main conclusion is that an increase of the forcing amplitude and a decrease of the upstream flow velocity lead to higher vectoring angles, similarly to the jet vectoring effects found in Smith & Glezer (2002). The increase of the deviated flow is then further correlated to a larger base pressure recovery and drag reduction.

It is additionally found that high-frequency actuation reduces the streamwise shear-layer growth and the cross-stream dynamics along the wake, resulting in a lower entrainment of external, high momentum fluid, in the recirculating bubble. By coupling the flow deviation and the overall damping of the velocity fluctuations, the bluff body drag is reduced by about 10 % at a Reynolds number  $Re_H = 3.0 \times 10^5$ .

While the low-frequency actuation is of the same order as the unforced vortex shedding, drag reduction takes place at time-scales one order of magnitude smaller, decoupled to the absolute instability of the wake (Huerre & Monkewitz 1990; Glezer *et al.* 2005). When compared to the shear-layer instabilities, the high-frequency forcing is roughly 3-4 times greater. Generally, these results show similar trends when compared to previous applications of high-frequency forcing in other shear flow configurations (Dandois *et al.* 2007; Vukasinovic *et al.* 2010; Oxlade *et al.* 2015).

A parallel between both actuation methods is made by analyzing their effects on the flow topology. The high-frequency forcing impacts the wake by two main process. An initial flow deviation close to the edges is responsible to narrow the entire wake. Besides, the periodic vortex train stabilizes the shear-layer implying an overall reduction of the wake turbulent kinetic energy. These coupled effects result in a wake length similar to the reference flow. The reduced velocity fluctuations acts to elongate the bubble length and to reduce wake entrainment. Then, a mean bubble with a higher aspect ratio  $L_r/H^*$  appears due to the lower  $H^*$ , differently to the low actuation frequency where the enhanced flow fluctuations decreases  $L_r$ . This scenario is consistent to the ideas proposed by Gerrard (1966) and Roshko (1955, 1993a) some decades ago.

Finally, the addition of the Coanda effect to the actuator system not only preserves the unsteady features of control but also reinforces the flow deviation close to the model. The resulted adjustment of the pressure gradients along the wake is favorable to the base pressure recovery and decreases the drag by almost 20 % when actuation at high-frequencies is applied. The unsteady Coanda blowing analyzed here complement the well-known steady actuation used in road vehicle's drag reduction and paves the way for its future development.

In general, the physical mechanisms highlighted here provide some guidelines to forthcoming drag control strategies. As an example, one would envisage other fluidic devices such as synthetic jets or oscillators (Cattafesta & Sheplak 2011) coupled with the Coanda effect or tail geometries to increase performance. Systematic variation of the numerous parameters such as the Reynolds number, the jet slit thickness, the blowing angle and the Coanda geometry might add some information on the scaling laws necessary to further applications in real road vehicles. To conclude, we believe these results additionally improve our understanding on how bluff body drag varies with wake forcing, which is

crucial to find out novel control strategies and implementation, as the recent applications in feedback systems (Brunton & Noack 2015).

## Acknowledgements

We are deeply indebted for indispensable experimental support of J.M. Breux, R. Bellanger and P. Braud and for stimulating discussions with V. Parezanović and R. Li. The thesis of D.B is supported financially by PSA - Peugeot Citroën and ANRT in the context of the OpenLab Fluidics between the Institut Pprime and PSA - Peugeot Citroën (fluidics@poitiers). We thank J. Östh and S. Krajnović for supporting our experimental work with illuminating LES data of the same setup. The authors thank the funding of the Chair of Excellence - Closed-loop control of turbulent shear flows using reduced-order models (TUCOROM)- supported by the French Agence Nationale de la Recherche (ANR). Last, but not least, we acknowledge the many insightful suggestions from the referees leading to a substantial improvement of the manuscript.

## REFERENCES

- ABRAMSON, P., VUKASINOVIC, B. & GLEZER, A. 2011 Direct measurements of controlled aerodynamic forces on a wire-suspended axisymmetric body. *Exp. Fluids* **50** (6), 1711–1725.
- AHMED, S. R., RAMN, G. & FALTIN, G. 1984 Some salient features of the time averaged ground vehicle wake. *SAE Tech. Report. No. 840300, Society of Automotive Engineers, Inc., Warrendale, PA*.
- BALACHANDAR, S., MITTAL, R. & NAJJAR, F. M. 1997 Properties of the mean recirculation region in the wakes of two-dimensional bluff bodies. *J. Fluid Mech.* **351**, 167–199.
- BARROS, D. 2015 Wake and drag manipulation of a bluff body using periodic fluidic forcing. PhD thesis, École Nationale Supérieure de Mécanique et d’Aérotechnique (ENSMA).
- BARROS, D., BORÉE, J., NOACK, B. R. & SPOHN, A. 2015 Resonances in the forced turbulent wake past a 3D blunt body. *submitted*.
- BARROS, D., RUIZ, T., BORÉE, J. & NOACK, B. R. 2014 Control of a three-dimensional blunt body wake using low and high frequency pulsed jets. *Int. J. Flow Control* **6** (1), 61–74.
- BEARMAN, P.W. 1965 Investigation of the flow behind a two-dimensional model with a blunt trailing edge and fitted with splitter plates. *J. Fluid Mech.* **21** (02), 241–255.
- BIAU, D. 2012 Laminar-turbulent separatrix in a boundary layer flow. *Phys. of Fluids* **24** (3).
- BONNET, J.P., DELVILLE, J., GLAUSER, M.N., ANTONIA, R.A., BISSET, D.K., COLE, D.R., FIEDLER, H.E., GAREM, J.H., HILBERG, D., JEONG, J. *et al.* 1998 Collaborative testing of eddy structure identification methods in free turbulent shear flows. *Exp. Fluids* **25** (3), 197–225.
- BRUNTON, S.T. & NOACK, B. R. 2015 Closed-loop turbulence control: Progress and challenges. *Appl. Mech. Reviews* **67** (5), 050801.
- CATTAFESTA, L. N. & SHEPLAK, M. 2011 Actuators for active flow control. *Ann. Rev. Fluid Mech.* **43**, 247–272.
- CHALIGNÉ, S. 2013 Contrôle du sillage d’un corps non profilé: application expérimentale à une maquette simplifiée de véhicule industriel. PhD thesis, École Centrale de Lyon.
- CHALIGNÉ, S., CASTELAIN, T., MICHARD, M. & JUVÉ, D. 2013 Active control of the flow behind a two-dimensional bluff body in ground proximity. *Comptes Rendus Mécanique* **341** (3), 289–297.
- CHOI, H., JEON, W.P. & KIM, J. 2008 Control of flow over a bluff body. *Ann. Rev. Fluid. Mech.* **40**, 113–139.
- CHOI, H., LEE, J. & PARK, H. 2014 Aerodynamics of heavy vehicles. *Ann. Rev. Fluid. Mech.* **46**, 441–468.
- CHUN, K. B & SUNG, H. J. 1996 Control of turbulent separated flow over a backward-facing step by local forcing. *Exp. Fluids* **21** (6), 417–426.

- DABIRI, J.O. 2009 Optimal vortex formation as a unifying principle in biological propulsion. *Ann. Rev. Fluid Mech.* **41**, 17–33.
- DAHAN, J. A., MORGANS, A. S. & LARDEAU, S. 2012 Feedback control for form-drag reduction on a bluff body with a blunt trailing edge. *J. Fluid Mech.* **704**, 360–387.
- DANDOIS, J., GARNIER, E. & SAGAUT, P. 2007 Numerical simulation of active separation control by a synthetic jet. *J. Fluid Mech.* **574**, 25–58.
- ENGLAR, R. J. 2001 Advanced aerodynamic devices to improve the performance, economics, handling and safety of heavy vehicles. *SAE Tech. Report. No. 2001-01-2072, Society of Automotive Engineers*.
- FIEDLER, H. E. 1998 Control of free turbulent shear flows. In *Flow Control*, pp. 335–429. Springer.
- FREUND, J.B. & MUNGAL, M.G. 1994 Drag and wake modification of axisymmetric bluff bodies using coanda blowing. *J. Aircraft* **31** (3), 572–578.
- GERRARD, J. H. 1966 The mechanics of the formation region of vortices behind bluff bodies. *J. Fluid Mech.* **25**, 401–413.
- GHARIB, M., RAMBOD, E. & SHARIFF, K. 1998 A universal time scale for vortex ring formation. *J. Fluid Mech.* **360**, 121–140.
- GLEZER, A. & AMITAY, M. 2002 Synthetic jets. *Ann. Rev. Fluid. Mech.* **34** (1), 503–529.
- GLEZER, A., AMITAY, M. & HONOHAN, A. M. 2005 Aspects of low-and high-frequency actuation for aerodynamic flow control. *AIAA journal* **43** (7), 1501–1511.
- GRANDEMANGE, M., GOHLKE, M. & CADOT, O. 2013 Turbulent wake past a three-dimensional blunt body. part 1. global modes and bi-stability. *J. Fluid Mech.* **722**, 51–84.
- HO, C. M. & HUERRE, P. 1984 Perturbed free shear layers. *Ann. Rev. Fluid. Mech.* **16**, 365–422.
- HUCHO, W. H. & SOVRAN, G. 1993 Aerodynamics of road vehicles. *Ann. Rev. Fluid. Mech.* **25**, 485–537.
- HUERRE, P. & MONKEWITZ, P.A. 1990 Local and global instabilities in spatially developing flows. *Ann. Rev. Fluid. Mech.* **22** (1), 473–537.
- JUKES, T.N. & CHOI, K. S. 2009 Long lasting modifications to vortex shedding using a short plasma excitation. *Phys. Rev. letters* **102** (25), 254501.
- KRAJNOVIC, S. & DAVIDSON, L. 2003 Numerical study of the flow around a bus-shaped body. *J. Fluids Eng.* **125** (3), 500–509.
- KRENTTEL, D., MUMINOVIC, R., BRUNN, A., NITSCHKE, W. & KING, R. 2010 Application of active flow control on generic 3D car models. In *Active flow control II*, pp. 223–239. Springer.
- LAHAYE, A., LEROY, A. & KOURTA, A. 2014 Aerodynamic characterisation of a square back bluff body flow. *Int. J. Aerod.* **4** (1-2), 43–60.
- LITTLEWOOD, R. & PASSMORE, M. 2010 The optimization of roof trailing edge geometry of a simple square-back. *Tech. Rep.*. SAE Tech. Paper.
- LITTLEWOOD, R. P. & PASSMORE, M.A. 2012 Aerodynamic drag reduction of a simplified squareback vehicle using steady blowing. *Exp. Fluids* **53** (2), 519–529.
- MORRIS, S.C. & FOSS, J.F. 2003 Turbulent boundary layer to single-stream shear layer: the transition region. *J. Fluid Mech.* **494**, 187–221.
- MORRISON, J.F. & QUBAIN, A. 2009 Control of an axisymmetric turbulent wake by a pulsed jet. In *Advances in Turbulence XII*, pp. 225–228. Springer.
- ÖSTH, J., NOACK, B. R., KRAJNOVIĆ, S., BARROS, D. & BORÉE, J. 2014 On the need for a nonlinear subscale turbulence term in POD models as exemplified for a high-Reynolds-number flow over an Ahmed body. *J. Fluid Mech.* **747**, 518–544.
- OXLADE, A. R., MORRISON, J. F., QUBAIN, A. & RIGAS, G. 2015 High-frequency forcing of a turbulent axisymmetric wake. *J. Fluid Mech.* **770**, 305–318.
- PREZANOVIC, V. 2011 Experimental study of the sensitivity of global properties of turbulent bluff body wakes using steady disturbance methods. PhD thesis, École Polytechnique.
- PREZANOVIC, V. & CADOT, O. 2012 Experimental sensitivity analysis of the global properties of a two-dimensional turbulent wake. *J. Fluid Mech.* **693**, 115–149.
- PREZANOVIC, V., LAURENTIE, J.C., FOURMENT, C., DELVILLE, J., BONNET, J.P., SPOHN, A., DURIEZ, T., CORDIER, L., NOACK, B.R., M.ABEL *et al.* 2015 Mixing layer manipulation experiment. *Flow, Turbulence and Combustion* **94** (1), 155–173.
- PARK, H., LEE, D., JEON, W. P., HAHN, S., KIM, J., J.KIM, CHOI, J. & CHOI, H. 2006 Drag

- reduction in flow over a two-dimensional bluff body with a blunt trailing edge using a new passive device. *J. Fluid Mech.* **563**, 389–414.
- PASTOOR, M., HENNING, L., NOACK, B. R., KING, R. & TADMOR, G. 2008 Feedback shear layer control for bluff body drag reduction. *J. Fluid Mech.* **608**, 161–196.
- PFEIFFER, J. & KING, R. 2012 Multivariable closed-loop flow control of drag and yaw moment for a 3d bluff body. *Proceedings of the 6th AIAA Flow Control Conference*.
- PHILIP, J. & MARUSIC, I. 2012 Large-scale eddies and their role in entrainment in turbulent jets and wakes. *Phys. Fluids* **24** (5), 055108.
- PRASAD, A. & WILLIAMSON, C. H. K. 1997 The instability of the shear layer separating from a bluff body. *J. Fluid Mech.* **333**, 375–402.
- RASPA, V., GODOY-DIANA, R. & THIRIA, B. 2013 Topology-induced effect in biomimetic propulsive wakes. *J. Fluid Mech.* **729**, 377–387.
- RIGAS, G., OXLADE, A.R., MORGANS, A.S. & MORRISON, J.F. 2014 Low-dimensional dynamics of a turbulent axisymmetric wake. *J. Fluid Mech.* **755**, R5.
- ROSHKO, A. 1955 On the wake and drag of bluff bodies. *J. Aeronautical Sciences* **22** (2).
- ROSHKO, A. 1993a Free shear layers, base pressure and bluff-body drag. *Tech. Rep.*. DTIC Document.
- ROSHKO, A. 1993b Perspectives on bluff body aerodynamics. *J. Wind Engng. Ind. Aerod.* **49** (1), 79–100.
- ROUMEAS, M., GILLIÉRON, P. & KOURTA, A. 2009 Analysis and control of the near-wake flow over a square-back geometry. *Computers & Fluids* **38** (1), 60–70.
- RUIZ, T., SICOT, C., BRIZZI, L. E., LAUMONIER, J., BORÉE, J. & GERVAIS, Y. 2009 Unsteady near wake of a flat disk normal to a wall. *Exp. Fluids* **47** (4-5), 637–653.
- SMITH, B.L. & GLEZER, A. 1998 The formation and evolution of synthetic jets. *Phys. Fluids* **10** (9), 2281–2297.
- SMITH, B.L. & GLEZER, A. 2002 Jet vectoring using synthetic jets. *J. Fluid Mech.* **458**, 1–34.
- SMITH, B.L. & GLEZER, A. 2005 Vectoring of adjacent synthetic jets. *AIAA journal* **43** (10), 2117–2124.
- SPOHN, A. & GILLIÉRON, P. 2002 Flow separations generated by a simplified geometry of an automotive vehicle. *IUTAM Symposium: Unsteady Separated Flows*.
- SYCHEV, V.V. 1982 Asymptotic theory of separation flows. *Fluid Dynamics* **17** (2), 179–188.
- VOLPE, R., DEVINANT, P. & KOURTA, A. 2015 Experimental characterization of the unsteady natural wake of the full-scale square back ahmed body: flow bi-stability and spectral analysis. *Exp. Fluids* **56** (5), 1–22.
- VUKASINOVIC, B., RUSAK, Z. & GLEZER, A. 2010 Dissipative small-scale actuation of a turbulent shear layer. *J. Fluid Mech.* **656**, 51–81.
- WASSEN, E., EICHINGER, S. & THIELE, F. 2010 Simulation of active drag reduction for a square-back vehicle. In *Active Flow Control II*, pp. 241–255. Springer.
- WEST, G.S. & APELT, C.J. 1982 The effects of tunnel blockage and aspect ratio on the mean flow past a circular cylinder with reynolds numbers between  $10^4$  and  $10^5$ . *J. Fluid Mech.* **114**, 361–377.
- WILLE, R. & FERNHOLZ, H. 1965 Report on the first european mechanics colloquium, on the coanda effect. *J. Fluid Mech.* **23** (04), 801–819.